DEVELOPMENT AN IMPREGNATION METHODOLOGY BY SPRAY COATING TO PREPARE SOFC CATHODES OF COMPOSITION (Y,Zr)MnO_3 ON YSZ SCAFFOLDS.

OMAR ADOLFO ROJAS GARCIA

IN PARTIAL FULFILLMENT OF THE REQUIREMENTS OF THE DEGREE OF MASTER IN MATERIALS ENGINEERING

ADVISOR

FERNANDO VIEJO ABRANTRE

Ph.D. MATERIAL SCIENCE AND TECHNOLOGY

CO-ADVISORS

Ph.D. GILLES GAUTHIER

Ph.D. JUAN SEBASTIAN VECINO MANTILLA

UNIVERSIDAD INDUSTRIAL DE SANTANDER

FACULTAD DE INGENIERÍAS FISICOQUÍMICAS

ESCUELA DE INGENIERÍA METALÚRGICA Y CIENCIA DE LOS MATERIALES

MAESTRÍA EN INGENIERÍA DE LOS MATERIALES

BUCARAMANGA

2026

Dedication

This study is wholeheartedly dedicated to my beloved parents, and family, who are a source of inspiration and gave me strength every step of the way.

I would like to dedicate this achievement to Adolfo Leon Garcia and Pedro Felix Rojas, I know you watching over me from heaven. Thanks for all the hard work and values you taught me, I miss you deeply.

Lastly, to myself: this journey was not easy. There were many moments of doubt, but it is finally over.

Acknowledgements

First and foremost, I would like to thank Dr. **Fernando Viejo**, Dr **Gilles Gauthier**, and Dr. **Sebastian Vecino** the opportunity they have given me to realize my Master Thesis. They have oriented and guided me in the world of research.

I would also like to thank all the members of the group **INTERFASE**: Isaac Hernandez, Laura Peñuela, Laura Pinto, Valentina Quintero, Andres Ramirez, Julian Guerrero, Karol Sandoval and Dr. Debora Nabarlatz. They have not only offered me advise on the academic point of view but also, they share the difficulties of COVID-19 and the departure of our first advisors. This could not have been done without them.

At the same time, my sincere appreciation to my dear friends, Angie Marin, Natalia Gallo, Melisa Estévez, Sebastian Ceballos, Michelle Cedeño and Vianny Gutierrez, who teach me the value of real friendship and had help me in different ways through this journey. To my partner, thank you for your love and dedication for standing by me in my darkest moments, and for helping me see the whole path clearly.

Additionally, during this journey I had the privilege of meeting the teachers Leidy Perez, Yeimi Guerrero, and William Cardenas, as well as the students Evann and Isabella, who reminded me of my passion for knowledge.

Sincere appreciation is extended to Dr. **Carlos Alberto Rios Reyes** from the Laboratorio de Microscopía, Parque Tecnológico de Guatiguará, Universidad Industrial de Santander, for his excellent assistance with SEM/EDS analyses; Dr. **José Antonio Henao Martínez** from the Laboratorio de Difracción de Rayos X, Parque Tecnológico de Guatiguará, Universidad Industrial de Santander, for his excellent assistance with XRD analyses.

TABLE OF CONTENT

Pag.

LIST OF TABLES

LIST OF FIGURES

Pag.

List of Appendices

List of Abbreviations

BSCF	Barium strontium cobalt ferrite
BSED	Backscattered electron detector
EDS	Energy dispersive spectroscopy
GDC	Gadolinium doped ceria
IT-SOFC	Intermediate temperature solid oxide fuel cell
IWI	Incipient wetness impregnation
LSC	Lanthanum strontium cobaltite
LSCF	Lanthanum strontium cobalt ferrite
LSF	Lanthanum strontium ferrite
LSM	Lanthanum strontium manganite
MIEC	Mixed ionic and electronic conductor
Ni-GDC	Nickel - Gadolinium doped ceria
Ni-YSZ	Nickel-Yttria stabilized zirconia
PAFC	Phosphoric acid fuel cell
PC-YSZ	Previously Calcinated - Yttria stabilized zirconia
PEM	Proton-exchange membrane
PV	Photovoltaics
PVA	Polyvinyl alcohol
PVB	Polyvinyl butyral
PVP	Polyvinyl pyrrolidone
SEM	Scanning electron microscope
SOFC	Solid oxide fuel cell
TEC	Thermal expansion coefficient
TEM	Transmission electron microscopy
TPB	Triple phase boundary
XRD	X-ray diffraction
YSZ	Yttria-stabilized zirconia
YZMO	Yttrium zirconium manganite
YZMO-1	Main yttrium zirconium manganite phase
YZMO-2	Secondary yttrium zirconium manganite phase

Resumen

Titulo: DESARROLLO DE UNA METODOLOGÍA DE IMPREGNACIÓN MEDIANTE RECUBRIMIENTO POR SPRAY PARA PREPARAR CÁTODOS DE SOFC DE COMPOSICIÓN (Y,Zr)MnO_3 SOBRE ANDAMIOS DE YSZ*

Autor: OMAR ADOLFO ROJAS GARCIA**

Palabras Clave: SOFC, Cátodo, Impregnación, Energías Renovables.

Descripción:

Las celdas de combustible de óxido sólido (SOFC) requieren catodos con alta conductividad iónica, compatibilidad química y una microestructura adecuada para lograr un desempeño electroquímico eficiente. En este trabajo se desarrolló una metodología de impregnación por spray coating para preparar cátodos de composición (Y,Zr)MnO_3 sobre scaffold de zirconia estabilizada con itria (YSZ). El estudio se llevó a cabo en dos etapas: primero, la formación de la fase (Y,Zr)MnO_3 mediante impregnación por humedad incipiente sobre polvo de YSZ; y segundo, la fabricación de scaffold porosos de YSZ depositados por spray coating sobre electrolitos densos, seguida de la impregnación del cátodo. Los polvos y scaffold de YSZ se sinterizaron a 1200 °C y 1300 °C (T_1), mientras que los materiales impregnados se trataron térmicamente entre 1000 °C y 1200 °C (T_2). La evolución de fases y los parámetros estructurales se analizaron mediante DRX con refinamiento Rietveld, mientras que las características microestructurales y la distribución elemental se examinaron por SEM y HAADF-EDS. Los resultados mostraron que la difusión de Zr desde el YSZ hacia el $YMnO_3$ promueve la formación de fases (Y,Zr)MnO_3 con contenido de Zr, siendo la estructura centrosimétrica $P6_3/mmc$ dominante a mayores temperaturas de síntesis. Los scaffold más finos y porosos obtenidos a menores temperaturas de sinterización favorecieron una mayor incorporación de Zr y una distribución de fases más homogénea. La metodología de impregnación por spray coating propuesta permite la formación controlada de (Y,Zr)MnO_3 dentro de scaffold de YSZ y demuestra el papel de la microestructura del scaffold en el cambio de la composición de fases y el potencial desempeño del cátodo en SOFC.

* Proyecto de grado

** Facultad de Ingenierías Fisicoquímicas. Escuela de Ingeniería Metalurgica. Universidad Industrial de Santander. Director: Fernando Viejo, Ph.D, Codirector: Gilles Gauthier, Ph.D, Sebastian Vecino, Ph.D

Abstract

Title: DEVELOPMENT AN IMPREGNATION METHODOLOGY BY SPRAY COATING TO PREPARE SOFC CATHODES OF COMPOSITION (Y,Zr)MnO_3 ON YSZ SCAFFOLDS.*

Autor: OMAR ADOLFO ROJAS GARCIA**

Palabras Clave: SOFC, Cathode, Impregnation, Renewable energy.

Description:

Solid oxide fuel cells (SOFCs) require cathode materials with high ionic conductivity, chemical compatibility, and suitable microstructure to achieve efficient electrochemical performance. In this work, an impregnation methodology by spray coating was developed to prepare (Y,Zr)MnO_3 cathodes on yttria-stabilized zirconia (YSZ) scaffolds. The study was conducted in two stages: first, the formation of the (Y,Zr)MnO_3 phase by incipient wetness impregnation on YSZ powder; and second, the fabrication of porous YSZ scaffolds deposited by spray coating over dense electrolytes, followed by cathode impregnation. YSZ powders and scaffolds were sintered at 1200 °C and 1300 °C (T_1), while the impregnated materials were thermally treated between 1000 °C and 1200 °C (T_2). Phase evolution and structural parameters were analyzed by X-ray diffraction with Rietveld refinement, whereas microstructural features and elemental distribution were examined by SEM and HAADF-EDS. Results showed that Zr diffusion from YSZ into $YMnO_3$ promotes the formation of Zr-containing (Y,Zr)MnO_3 phases, with the centrosymmetric $P6_3/mmc$ structure becoming dominant at higher synthesis temperatures. Finer and more porous scaffolds obtained at lower sintering temperatures favored deeper Zr incorporation and a more homogeneous phase distribution, while grain coarsening at higher T_1 limited Zr diffusion. The proposed spray-coating impregnation methodology enables controlled formation of (Y,Zr)MnO_3 within YSZ scaffolds and demonstrates the role of scaffold microstructure in tailoring phase composition and potential SOFC cathode performance.

* Degree work

** Faculty of Physical-chemical Engineering. School of Metallurgic Engineering. Universidad Industrial de Santander. Director: Fernando Viejo, Ph.D.; Co-director: Gilles Gauthier, Ph.D., Sebastian Vecino, Ph.D

1. Introduction

In recent years, energy demand has increased because of industrial expansion. Consequently, there is a growing depletion of fossil energy sources but also a drastic increase of environmental pollution, resulting from the emission of large amounts of CO_2 that is the main responsible of global warming (Moreno, 2018; Palakkathodi Kammampata, 2014). Those aspects have placed humanity on the need to seek alternative and efficient conversion devices that transform renewable fuels (biodiesel, biogas, hydrogen, and others) into energy to supply its global demand profitably (Parajón-Costa et al., 2003)

Power generation through fuel cells, explicitly using Solid Oxide Fuel Cells (SOFC), has been considered a remarkable technology since their efficiency values are theoretically higher than those of classical thermal machines, *e.g*. engines or turbines (Table 1.1) (Minh & Takahashi, 1995d). Moreover, SOFC systems have the advantage of working directly on the anode side with H_2, as well as various fuels such as hydrocarbons (alcohols, natural gas, biogas), synthesis gas, among others, and air on the cathode side (Mahato et al., 2015; Mekhilef et al., 2012)**.**

Table 1
Attributes of Selected Distributed Generation Systems. Taken from Fuel Cell Handbook (Energy and Environmental Solutions, 2000).

Type	Size	Efficiency [%]
Reciprocating Engines	50 kW – 6 MW	33-37
Microturbines	10 kW – 300 kW	20-30
Phosphoric Acid Fuel Cell (PAFC)	50 kW – 1 MW	40
Solid Oxide Fuel Cell (SOFC)	5 kW – 3 MW	45-65
Proton Exchange Membrane Fuel Cell (PEM)	<1 kW – 1 MW	34-36
Photovoltaics (PV)	1 kW – 1 MW	NA
Wind Turbines	150 kW – 500 kW	NA
Hybrid Renewable	<1 kW – 1 MW	40-50

SOFC are solid-stated energy conversion devices that transform chemical energy directly to electrical energy from the oxidation of a fuel, employing an oxidant gas. They operate in the temperature range of 700-1000°C (Energy and Environmental Solutions, 2000; Minh & Takahashi, 1995c; Tu & Stimming, 2004). The overall reaction is the same as that of the combustion; however, the reaction is constituted by two separate electrochemical reactions. When hydrogen (fuel) and oxygen (oxidant) are used, the electrochemical reaction consists of the oxidation of hydrogen at the anode (Eq. 1-1) and the reduction of oxygen at the cathode (Eq. 1-2).

Anode:

$$2H_2 + 2O^{2-} \leftrightarrow 2H_2O + 4e^- \qquad \textbf{Eq. (1-1)}$$

Cathode:

$$O_2 + 4e^- \leftrightarrow 2O^{2-} \qquad \textbf{Eq. (1-2)}$$

The diffusion of oxygen ions occurs through the electrolyte from the cathode to the anode side (see Figure 1). In the case of using hydrocarbon-based fuels different from hydrogen gas, there is a previous step of reforming before the oxidation that can be carried out in an external reactor or directly at the anode (Energy and Environmental Solutions, 2000; Minh & Takahashi, 1995c; Tu & Stimming, 2004).

Figure 1.
Operation Scheme of SOFC. Taken from Mahato, N. (2015) (Mahato et al., 2015).

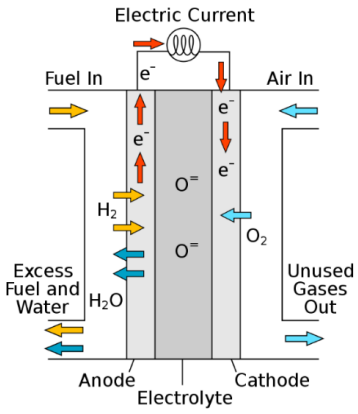

Table 2.
Components of SOFC. Adapted from Mahato, N. (2015)(Mahato et al., 2015).

Component	Material	General requirements
Anode	Cermet Ni/YSZ (Ni/ZrO_2 stabilized with Y_2O_3) Cermet Ni/GDC (Ni/CeO_2 stabilized with Gd_2O_3)	(i) High porosity to have a better catalytic activity and diffusion of the gas for oxygen reduction or fuel oxidation. (ii) Good chemical and thermal stability. (iii) Similar coefficient of thermal expansion as the electrolyte. (iv) High electronic conductivity and ionic conductivity under operation conditions to increase the surface area of the effective reaction zone and minimize the polarization losses. (v) Dimensional and thermodynamic stability over wide ranges of partial pressure of oxygen and temperature (from room temperature to 1000°C).
Cathode	$La_{1-x}Sr_xMnO_3$ (LSM) $Ba_{0.5}Sr_{0.5}CoO_3$ $La_{1-x}Sr_xCo_{1-y}Fe_yO_3$	
Electrolyte	YSZ (ZrO_2 stabilized with Y_2O_3) GDC (CeO_2 stabilized with Gd_2O_3)	(i) Elevated oxide ion conductivity at operating temperature (~0.1 S/cm). (ii) Low electronic transference number ($<10^{-3}$). (iii) Chemical inertness toward electrode materials. (iv) Coefficient of thermal expansion compatible with electrode materials and interconnectors. (v) Stable structure throughout the thermal cycle of the device. (vi) High density (>90%) to avoid interconnected porosity. (vii) Ability to withstand a wide range of oxygen partial pressure ($1\text{-}10^{-22}$ atm).

As exposed in Table 2, the materials of SOFC components must exhibit some specific characteristics. In the case of the electrodes, it is important to achieve a notable catalytic activity

(anode), as well as excellent electrochemical properties in terms of low polarization for the H_2 electrochemical oxidation at the anode, and the reduction of oxidant agent at the cathode. Such a combination is essential for a long-term operation of these devices at high temperatures (700-1000°C) (Minh & Takahashi, 1995a; Parajón-Costa et al., 2003; Singhal & Kendall, 2003).

Nevertheless, one of the main issues that SOFC technology faces is its high cost of production, which is a consequence of the difficulty in finding and producing the constituent materials (especially the electrodes) (Minh & Takahashi, 1995b; Zhang et al., 2017). In particular, the cathode is typically a noble metal or a complex oxide, whose high cost is a critical restriction for the application on a larger scale. Therefore, researchers have been focusing their investigations on the study and characterization of perovskite-type ABO_3 oxide (Figure 2) (Ishihara, 2009) as potential cathode materials in these cells.

Figure 2.
ABO_3 perovskite structure. Adapted from Sun, C. et. Al. (2010)(Sun et al., 2010)

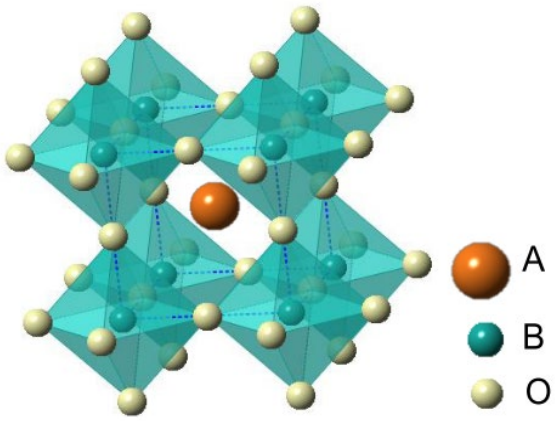

In this regard, one of the most studied compounds for SOFC cathode application has been $LaMnO_3$, which exhibits a thermal expansion coefficient (TEC) of 11 x 10^{-6} K^{-1}, similar to the values of the most common electrolytes (*i.e.* YSZ) (Minh & Takahashi, 1995a; Sun et al., 2010)

and it is stable in an oxidizing atmosphere. This oxide has been taken as the base for different substitutions of lanthanum cations to enhance the oxygen nonstoichiometric and oxygen defects, resulting in the general formula $La_{1-x}A_xMnO_{3\pm\delta}$. Specifically, it has been demonstrated that the substitution of La^{3+} for Sr^{2+} in $La_{1-x}Sr_xMnO_3$ ($x<0.5$) causes the oxidation of manganese cations, increasing the concentration of electronic holes, and therefore improving the electrical conductivity (Sandoval et al., 2017). However, to obtain good electrochemical performance in cathode conditions, the cell needs to be operated above 800°C (Mizusaki et al., 2000). Unfortunately, under such conditions, some authors reported microstructural and structural degradation due to grain growth and the reactivity between phases (Sun et al., 2010). Further, at higher temperatures (cathode fabrication temperature), *i.e.*, 1200 °C, the greater presence of oxygen defects promotes the reactivity of the LSM perovskite with the YSZ electrolyte resulting in the formation of $La_2Zr_2O_7$ and $SrZrO_3$ that insulates phases at the interface with YSZ electrolyte. Nevertheless, this aspect can be partially prevented by limiting the molar concentration of Sr between 10-20% (Chen et al., 2015; Mitterdorfer & Gauckler, 1998; Stochniol et al., 1995).

On the other hand, since LSM is a purely electronic conductor with poor electrochemical activity, several studies have been carried out to convert LSM into a mixed conductor or MIEC (Mixed Ionic and Electronic Conductor), which is considered as the ideal electrode active material. Conventionally, the electronic conductivity of the LSM materials is restricted to the contacts between the ionic conducting phase (the YSZ electrolyte), the electronic conducting phase (LSM), and the pore, as established by the species that participate in the diffusion of oxygen ions through the cell (Sun et al., 2010). This zone is called the triple-phase limit boundary or TPB (Figure 3a). In turn, the MIEC material extends the reaction zones in the whole electrode volume (Figure 3b), allowing the operation at intermediate temperature (600-800°C) (IT-SOFC)(Jiang, 2006a;

Moreno, 2018; Sun et al., 2010). Such a reduction in temperature allows to drastically decrease the degradation of the cell.

Figure 3.
Mobility of charge carriers in an electrode based on a) Electronic conductor and b) MIEC conductor (ionic and electronic).

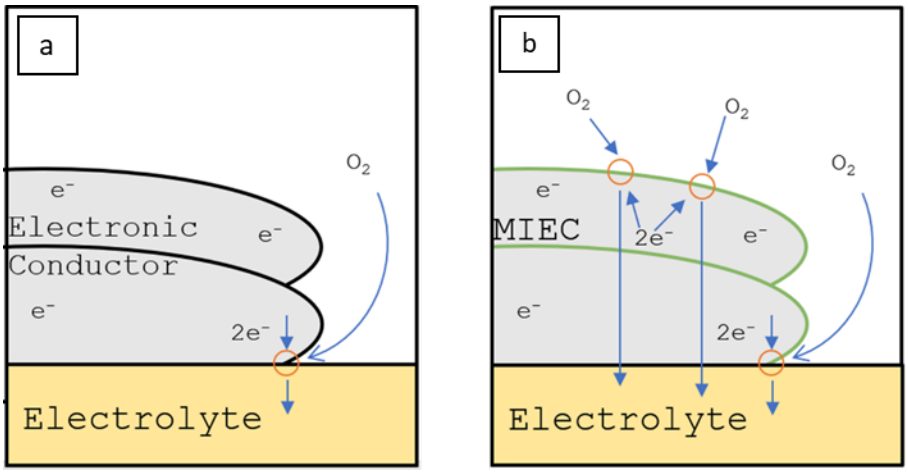

Note: Adapted from Kim, 2013(Kim et al., 2013).

The latter is possible through the partial or total substitution of the B site (Mn) with other more active transition metals (Kawada, 2009). One of the most promising MIEC is a cobaltite of the type $La_{1-x}Sr_xCoO_{3-\delta}$ (formed by the complete substitution of Mn by Co), which exhibits a greater oxygen diffusivity than LSM due to the substantial number of oxygen vacancies (expressed by non-stoichiometry in oxygen, δ) that results in a remarkable electronic conductivity. Nonetheless, the TEC of the cobaltite is almost twice the value for YSZ, which makes them incompatible with most electrolytes. In addition, at the high temperatures (>900°C) required for the cell elaboration, these materials tend to react forming insulating phases between the electrode and electrolyte that block the cathodic reaction (Sun et al., 2010).

Alternatively, scientists have produced ferrites by substitution of Mn with Fe ($La_{1-x}Sr_xFeO_3$) that exhibit lower TEC than cobaltites but display a decrease in electronic

conductivity (Bernardo & Vert Belenguer, 2011). To combine the excellent oxygen diffusivity of the cobaltites and the improved TEC of the ferrites, a ferro-cobaltite perovskite with composition $Ba_{0.5}Sr_{0.5}Co_{0.8}Fe_{0.2}O_3$ (BSCF) was investigated, being undoubtedly one of the best MIEC materials employed in IT-SOFC as cathode (Shen & Lu, 2016; Wang et al., 2009). However, the use of this material is difficult since its TEC is still too high ($20x10^{-6}$ K^{-1}, while YSZ is $11.5x10^{-6}$ K^{-1}) (Doleker et al., 2018; Wei et al., 2006), which could cause delamination problems, breakage, and a low contact area between the cathode and the electrolyte(Duan et al., 2006a; Shen & Lu, 2015). Consequently, the development of new cathode materials that may overcome the shortcomings of the currently used ones is still a big challenge.

In 2018, the INTERFASE group from the Industrial University of Santander (UIS) proposed the synthesis of new MIEC materials based on Zr-doped manganites with substitution of La element by Y, *i.e*. the (Y,Zr)MnO_3) family (Moreno Botello et al., 2017, 2019; Moreno, 2018) (Figure 4).

Figure 4.
Representation of hexagonal $YMnO_3$ structure. Buckled layers of Y atoms (black) in 8-fold coordination of O atoms (light grey) separate the [MnO_5] trigonal bi-pyramids (dark grey) layers in which each polyhedron is linked to three others by their equatorial planes. Taken from Moreno, Z.(2017) (Moreno Botello et al., 2017)

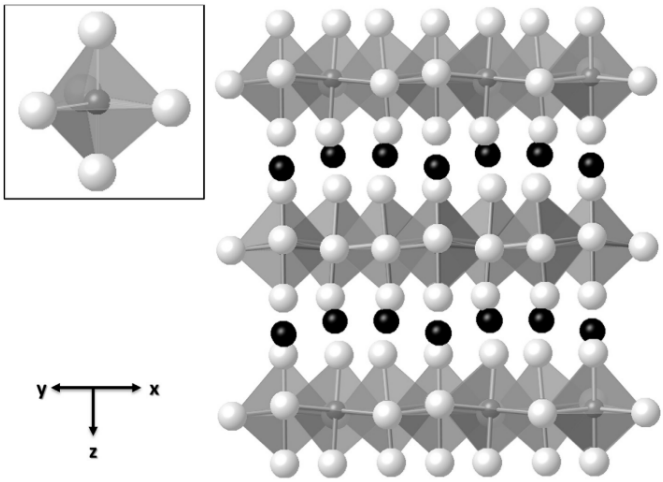

These materials are presented as exciting candidates for SOFC cathodes, since yttrium prevents the chemical reactivity with the YSZ electrolyte, unlike other materials containing Ba, Sr, and La. Moreover, the smaller ionic radius of yttrium modifies the cell structure from perovskite-type into a layer-type arrangement with additional atoms of oxygen in the layers and an increasing disorder in the tilting of Mn-O polyhedral, which could be associated with higher oxygen mobility(Duan et al., 2006b; Shen & Lu, 2015). The results obtained in this work showed that the $Y_{0.9}Zr_{0.1}MnO_{3.05}$ phase exhibits higher total electrical conductivity and higher ionic conductivity than pure $YMnO_3$. As a drawback, its impedance response is less favorable, indicating that this compound is not only affected by its transport properties but also by the microstructure obtained (Moreno, 2018).

As a consequence, it is necessary to investigate other methods for the cathode preparation that allow obtaining a very fine microstructure to reduce the high electrochemical resistance values of these electrodes. Accordingly, in recent years, the impregnation method has been highlighted as a particularly efficient strategy for preparing high-performance SOFC cell electrodes (Bezemer et al., 2006; Fan et al., 2018; Zhao et al., 2011). It consists of the preliminary preparation of a porous layer of electrolyte material (scaffold) deposited over a dense electrolyte, both sintered at high temperatures (>1000°C). The scaffold is impregnated with a precursor solution of the electrode material but now calcinated at a lower temperature to obtain a single-phase electrode with a high surface area. As a result, the polarization resistance in the electrode decreases, minimizing all the phenomena associated with the surface of the grains, particularly the phenomena of adsorption/dissociation and surface migration (Fan et al., 2018; Osinkin et al., 2015; Sholklapper et al., 2007).

Previous studies have demonstrated that impregnation into scaffolds can substantially enhance electrode performance. For example, GDC impregnation has been shown to improve both LSM-based cathodes and Ni-based anodes, achieving electrocatalytic activities comparable to state-of-the-art MIEC electrodes such as LSCF and GSC, as well as to conventional Ni/YSZ cermet anodes (Jiang, 2006b).

Therefore, the use of the impregnation method in materials such as $YMnO_3$ and $Y_{0.9}Zr_{0.1}MnO_3$ could potentially lead to a drastic improvement in their electrocatalytic properties (Moreno Botello et al., 2019).

Based on the information presented above, the present research work has been directed to study the implementation of the impregnation technique to obtain a (Y,Zr)MnO_3 phase within a YSZ scaffold. The first part of the investigation was focused on studying the synthesis of (Y,Zr)MnO_3 by impregnation on YSZ powder, followed by the development and characterization of the (Y,Zr)MnO_3 by impregnation over a sprayed YSZ scaffold.

2. Objectives

2.1. General Objective

To develop SOFC cathodes of composition (Y,Zr)MnO_3 on YSZ scaffolds employing an impregnation methodology by spray coating.

2.2. Specific Objectives

- To determine the preliminary conditions of the impregnation/calcination process of an 8YSZ powder to form a phase (Y,Zr)MnO_3.
- To evaluate the conditions for the scaffold formation over dense electrolyte by spray-coating.
- To determine the impregnation and calcination temperatures to get the (Y,Zr)MnO_3 cathode over a porous 8YSZ scaffold.

3. Methodology

Figure 5 presents the methodology sequence considered in the current investigation. Each step illustrated in the figure represents a specific objective and its respective parameter that was measured.

Figure 5.
Flowchart of the sequence used in this thesis to form the (Y,Zr)MnO_3 phase on the YSZ electrolyte.

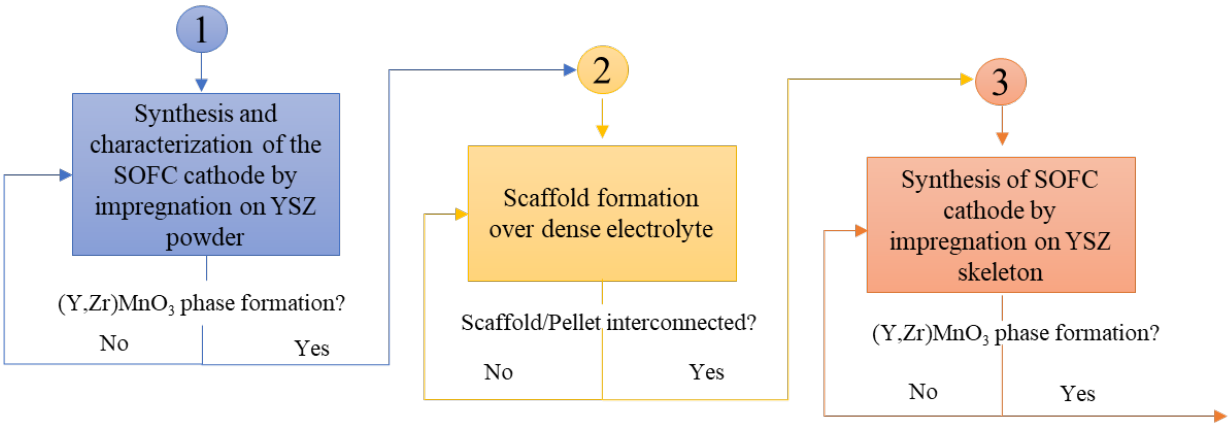

3.1 Synthesis and characterization of the SOFC cathode by impregnation on YSZ powder

Figure 6 shows the different steps followed for the synthesis of the (Y,Zr)MnO_3 cathode on YSZ powder.

.

Figure 6.
Sequence used for the synthesis of SOFC cathode by impregnation on YSZ powder: 1. Calcination of YSZ powder, 2. Preparation of precursor solution, 3. Impregnation of YSZ powder by IWI method, 4. Characterization of YSZ/ (Y,Zr)MnO_3 phase.

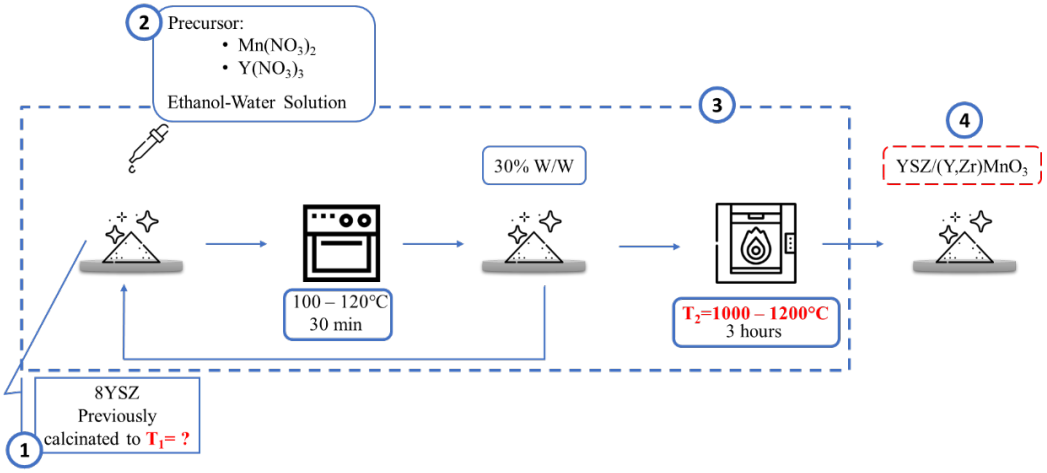

3.1.1 Pre-calcination of YSZ powder

Initially, commercial YSZ (YSZ-U1, Fuel Cell Materials, Ohio, USA) was analyzed by dilatometry to determine the range of temperature in which the powder has to be sintered with the aim to obtain the scaffold. For that purpose, a dilatometer DIL402C Netzsch was employed using a temperature range from 25°C to 1600°C and a heating rate of 300°C/h^{-1}. The temperatures for the calcination of YSZ powder T_1 were selected considering these results.

The calcination process of YSZ powder was carried out for 3 h at each temperature. The calcinated samples (referred to as PC-YSZ) were then analyzed by X-ray diffraction (XRD) to check their purity and determine/refine their structure (Moreno, 2018). The patterns were obtained using a diffractometer Bruker D8 Advance with DaVinci geometry operated in Bragg-Brentano geometry, equipped with a Lineal LynxEye detector and a beam of CuK$\alpha_{1,2}$ radiation (λ= 1.5418 Å). The system was operated over the angular range 2θ = 5 - 120° for the pattern qualitative analysis with a measurement step of 0.02035° (2θ). Rietveld analysis was performed using Jana 2006 software (Petříček et al., 2014). The results obtained were used as a blank for further analysis

of impregnated materials. On the other hand, the specimens were analyzed by Scanning Electron Microscopy (SEM) on Instrument Quanta FEG 650 to observe the influence of the thermal treatment (calcination) on YSZ grain size and microstructure. The powders were placed on metallic stubs with carbon duct tape, then coated with gold and placed on the microscope. The analysis was performed under a high vacuum atmosphere with an accelerating voltage of 25 keV with Everhart Thornley Detector (ETD) and backscattered electron detector (BSED) type SSD. The calcinated powders were subsequently employed as the scaffold in which the impregnation process was studied.

3.1.2 Preparation of $YMnO_3$ precursor solution

The precursor solution of $YMnO_3$ was prepared by mixing yttrium nitrate ($Y(NO_3)_3$) and manganese nitrate ($Mn(NO_3)_2{\cdot}5H_2O$, ≥ 99.9 % Merck) in a 50-50 v/v mixture of ethanol/water; the final amount of $YMnO_3$ in the solution was set at 10.58 (%w/w).

To obtain $Y(NO_3)_3$ solution, a powder of yttrium oxide (Y_2O_3, ≥ 99.9 % Alfa Aesar) was previously calcinated at 1000 °C in air at atmospheric conditions for 1 hour in a commercial muffle to remove humidity and impurities sorbed on the surface. Then, the formation of $Y(NO_3)_3$ was performed using stoichiometric amounts of the calcinated Y_2O_3 and HNO_3 (≥ 65 % Merck) in a beaker heated at 70 °C and stirred until dissolution (see Appendix A). The as-produced $Y(NO_3)_3$ was then diluted in distilled water to obtain a 1 M aqueous solution.

Additionally, $Mn(NO_3)_2{\cdot}5H_2O$ was also calcinated at 700 °C (Jian et al., 2014) to determine the exact weight to prepare a 1 M solution of $Mn(NO_3)_2$. Ethanol was employed as solvent

3.1.3 Impregnation of YSZ powder

The amount of $YMnO_3$ impregnated into the YSZ electrolyte was fixed to 30% w/w in agreement with the literature, being a minimum for the efficiency of the cell calculated from the amount of $YMnO_3$ solution infiltrated on 10 g of YSZ cell (Vohs & Gorte, 2009; Yuan et al., 2014) (see Appendix B). First, the incipient volume of YSZ powder was determined by adding distilled water to the previously calcinated YSZ (PC-YSZ) until the support had been saturated ("muddy" appearance). After knowing the incipient volume of the PC-YSZ and the total volume of precursor solution to be used, the number of impregnations was determined. Multiple impregnations were necessary due to the high loading required of $YMnO_3$.

The Incipient Wetness Impregnation (IWI) was performed on the previously calcinated YSZ powder adding the $YMnO_3$ precursor solution with a transfer pipette and then dried at 120°C for 30 min. This process was performed numerous times to achieve a high loading of the $YMnO_3$. Subsequently, the impregnated material was fired at 700°C for 1 h in air to convert the nitrates into oxides. Finally, the impregnated YSZ was heat treated at different temperatures, 1000, 1100, and 1200°C, called T_2, to examine the influence of the temperature on the formation of the desired phase. These temperatures were chosen based on previous studies carried out in the INTERFASE research group, in which it was demonstrated that the formation of (Y,Zr)MnO_3 begins from 1100°C using a sol-gel method (Moreno, 2018); 1000°C was also considered to evaluate the possibility whether the temperature of synthesis can be lowered by using the impregnation method.

3.1.4 Characterization of the YSZ/$YMnO_3$ composite material

Each synthesized powder was characterized by XRD, as mentioned in section 3.1.1, to observe the formation of the new phases and determine/refine their crystal structure. The diffractometer was operated over the angular range 2θ = 10-120° with a measurement step of

0.02035° (2θ) for the qualitative analysis and Rietveld analysis using Jana 2006 software (Petříček et al., 2014).

3.2 Preparation and characterization of the scaffold over dense electrolyte

In this second part of the methodology, and considering the results of the previous section, the formation of the scaffold over the dense electrolyte was studied. The steps are shown in Figure 7.

Figure 7.
Sequence used for the formation of the scaffold over the dense electrolyte. 1. Formation of the dense electrolyte, 2. Deposition of the scaffold over dense electrolyte, 3. Characterization of the framework

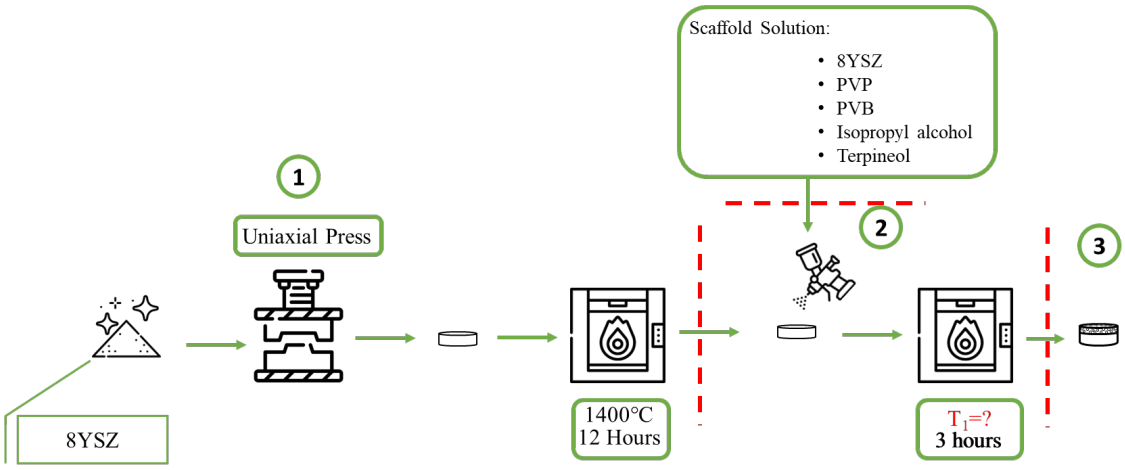

3.2.1 Formation of the dense electrolyte

The raw materials for the dense electrolyte were 8 mol% YSZ powder (YSZ-TC, Fuel Cell Materials, Ohio, USA (powder)) and polyvinyl alcohol (PVA) (99+% hydrolyzed, Merck, Germany). The PVA concentration in the dense electrolyte was established at 2.5% w/w, since it has been reported that a concentration higher than 3% w/w promoted a microstructure with high than 12 vol% of porosity, which is not needed for this application (Mudinepalli et al., 2013)(Batool

et al., 2018). First, YSZ powder was mixed with a PVA solution in water to form a slurry. This slurry was placed in the oven at 110°C for 3 hours to obtain a dry powder and then ground in a mortar to get a fine powder. Finally, this powder was pressed into pellets (Specac mold 15mm Ø and CARVER press 9000 psi) and sintered at 1400 °C for 12 hours with a heating ramp of 300°C $hour^{-1}$ (CARBOLITE furnace). The sintered pellets were polished on a diamond disk (MD-PIANO 220, HV150-2000, SiC grit 220) at 300 rpm for 60 seconds.

3.2.2 Preparation of the scaffold suspension

The suspension used for spray coating was prepared by mixing YSZ ceramic powder with isopropyl alcohol (99.9%, Panreac AppliChem), α-terpineol (for synthesis, Merck), polyvinylpyrrolidone (PVP, M_w:8000, Sigma Aldrich) and polyvinyl butyral (PVB, M_w:70000-100000, Sigma Aldrich) in a weight ratio of 35: 38.750: 23.625: 0.875: 1.750 (Moreno Botello et al., 2019)(Setevich et al., 2018). Initially, isopropyl alcohol and α-terpineol were mixed with an ultrasonic mixer (T 25 digital ULTRA-TURRAX, 21000 rpm) for one minute. Once well mixed, PVB, PVP and YSZ powders were added and mixed for 0.5 h until a suspension was formed (Tarasi et al., 2019).

3.2.3 Preliminary studies of deposition

With the aim to define the parameters for the spray deposition, preliminary studies were conducted. These studies focused on evaluating the stability of the solution, and the deposition time. To assess these parameters, first two solutions were prepared and aged for different durations, one fresh and the other for 24 h. Spray depositions of both solutions were then performed, lasting 2, 3, 4, and 5 s.

The surface of the resultant scaffolds was then observed by confocal microscopy (HIROX KH-7700) and SEM. After establishing the parameters of stability of the solution and deposition duration, the sintering process was evaluated by subjecting the scaffold to firing durations of 3 and 24 hours, respectively, and evaluating the evolution of scaffold after the thermal treatment.

3.2.4 Deposition of the porous electrolyte over the dense electrolyte

Once the suspension was ready, it was sprayed over the ground side of the pellet with a SATA jet 5000 airbrush positioned 21 cm from the pellet and operated at a pressure of 0.4 bar. Subsequently, the pellets were heat treated at 110°C for 30 min to evaporate the solvents. At last, the matrix porous/dense electrolyte was calcinated at the same T_1 temperatures mentioned in section 3.1.1 for 3, 6, 12, and 24 h to obtain the scaffold.

3.2.5 Characterization of the scaffold

Each matrix (pellet/scaffold) was analyzed using confocal microscopy and SEM, observing the influence of time on the scaffold sintering, *i.e.* the surface, as well as the connectivity between YSZ grains (network development).

3.3 Synthesis and characterization of the SOFC cathode

Finally, the preparation of the SOFC cathode was carried out by impregnation of the scaffold using the IWI method, adapting the best conditions found in Section 3.1 and following the steps shown in Figure 8.

Figure 8.

Sequence for the synthesis of the SOFC cathode over the porous electrolyte. The synthesis was performed by adapting the best conditions found in the section 3.1 to obtain a scaffold with 30% W/W of $YMnO_3$.

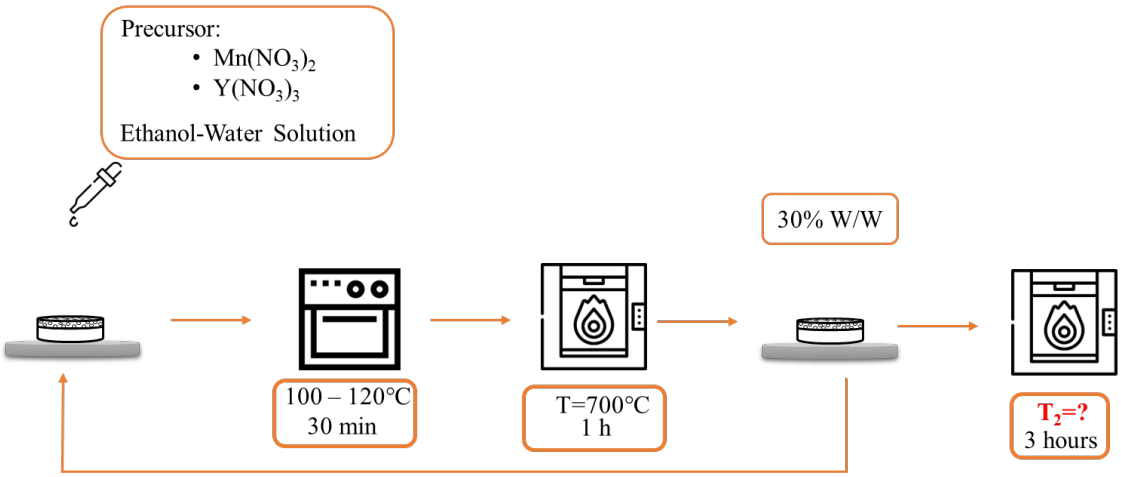

The amount of $YMnO_3$ impregnated into the YSZ electrolyte was set at 30% w/w (optimal proportion for fuel cell operation), calculated from the amount of $YMnO_3$ solution infiltrated into the YSZ scaffold. First, the IWI process was developed by meticulously adding the precursor solution drop by drop on the YSZ scaffold using a transfer pipette. The impregnated scaffold was dried at 120°C for 30 minutes between each drop. Subsequently, it was fired at 700°C for 1 hour in air. To conclude, the $YMnO_3$/YSZ material was heated at the T_2 temperatures selected in section 3.1.

The formation of the new phases over the scaffold was by Grazing Incidence X-ray diffraction (GIXRD). The patterns were obtained using a diffractometer Bruker D8 ADVANCE. The system was operated over the angular range $2\theta = 10 - 90°$ for the pattern qualitative analysis with the source angle 2°, and with a 1 mm slit.

4. Results

4.1 Synthesis by impregnation

The dilatometry curve of the commercial YSZ powder is shown in Figure 9. The powder starts to sinter at 1000°C approximately and this process ends at around 1600°C. Thus, the temperature for the scaffold formation should be ranged between 1000 and 1600°C. However, for the current study, two temperatures for the scaffold sintering (T_1) were fixed: 1200°C and 1300°C. Lower temperatures would produce finer grains with a limited connection, while scaffolds sintered at higher temperatures would not have sufficient porosity to carry out the impregnation step suitably (Song et al., 2018).

Figure 9.
Dilatometry curve of the commercial YSZ powder (YSZ-U1) from room temperature to 1600°C.

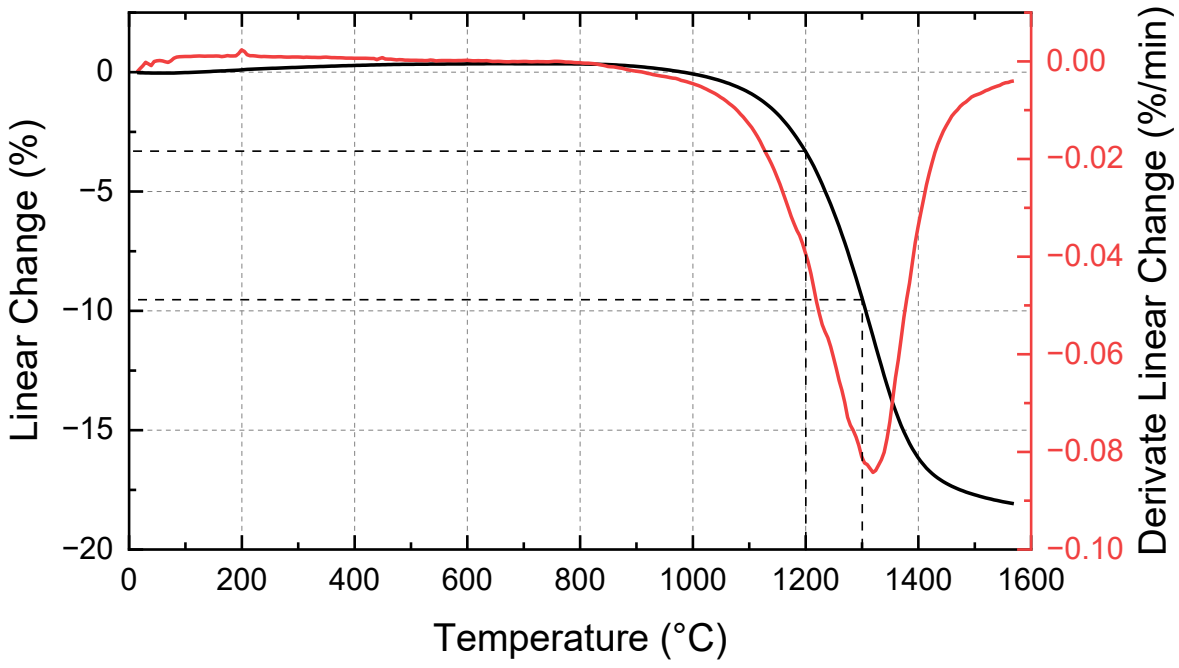

Complementarily, the SEM images disclosed in Figure 10 show the effect of the sintering process on YSZ powder. As expected, an increase in the sintering temperature leads to grain growth and promotes the connectivity between neighbouring particles.

Figure 10.
SEM analysis of the commercial YSZ powder: a) as-received, b) sintered at 1200 °C for 3 hours and c) sintered at 1300°C for 3 hours.

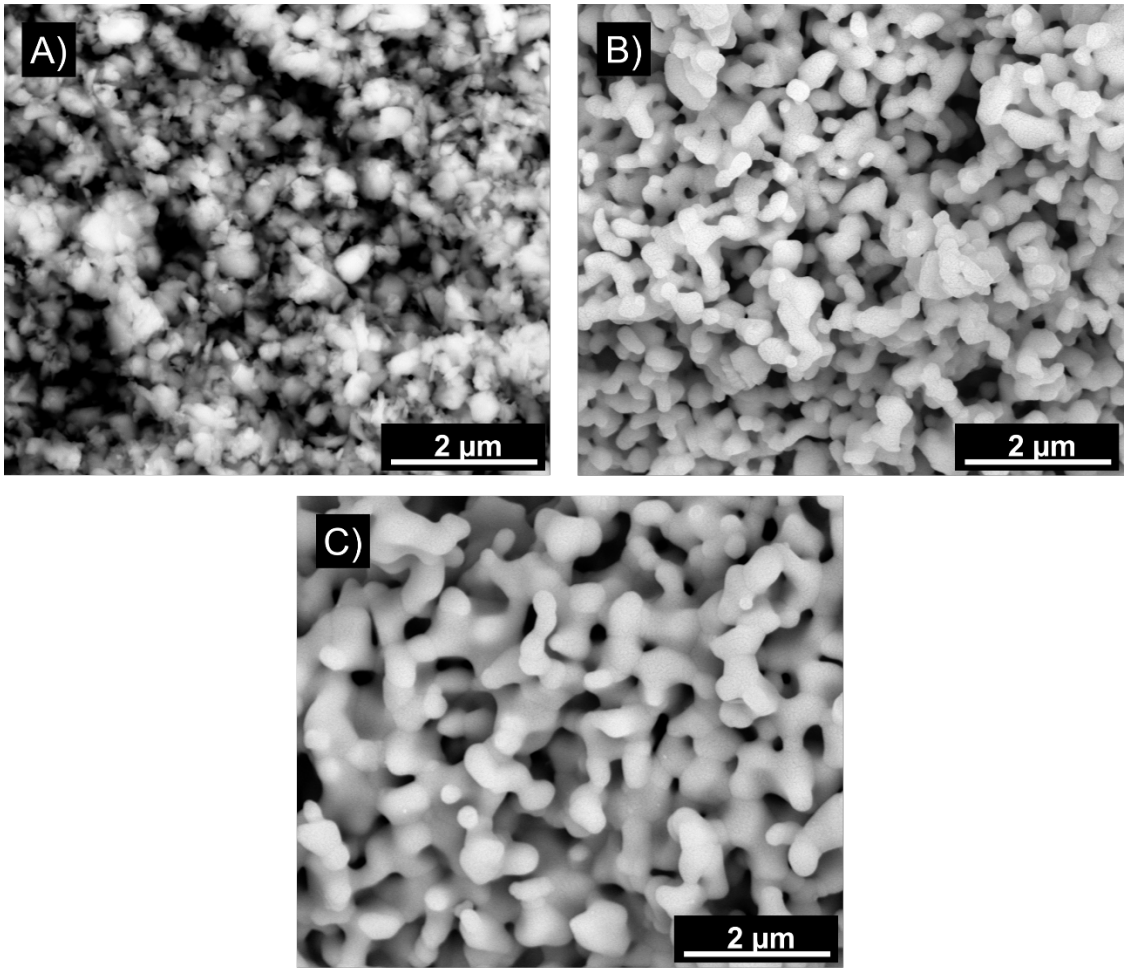

After establishing the parameters for the powder sintering, the followed step was the impregnation of it with a precursor solution of $YMnO_3$. Figure 11 shows the X-ray diffraction patterns of the material obtained, after sintering at T_1=1200°C for different synthesis temperatures (T_2)(1000-1200°C). For T_2=1000°C, the formation of a Zr-containing (Y,Zr)MnO_3 (YZMO-1) phase over the YSZ powder is observed (see Figure 11A), evidenced by a slight displacement in

2θ of the diffraction peaks for $YMnO_3$ pure phase(Moreno, 2018). However, an intermediate phase of YMn_2O_5 is also detected. This intermediate phase exhibits lower electronic conductivity hence it is not of interest for the present research (Gao et al., 2008; Noda et al., 2006). Nevertheless, the latter phase disappears at higher temperatures (T_2=1100°C-1200°C).

Figure 11.
X-ray diffraction pattern of A) $YMnO_3$ impregnated YSZ powder sintered at T_1=1200°C for different synthesis T_2 temperatures, B) zoom in the region 2θ=20°-40°.

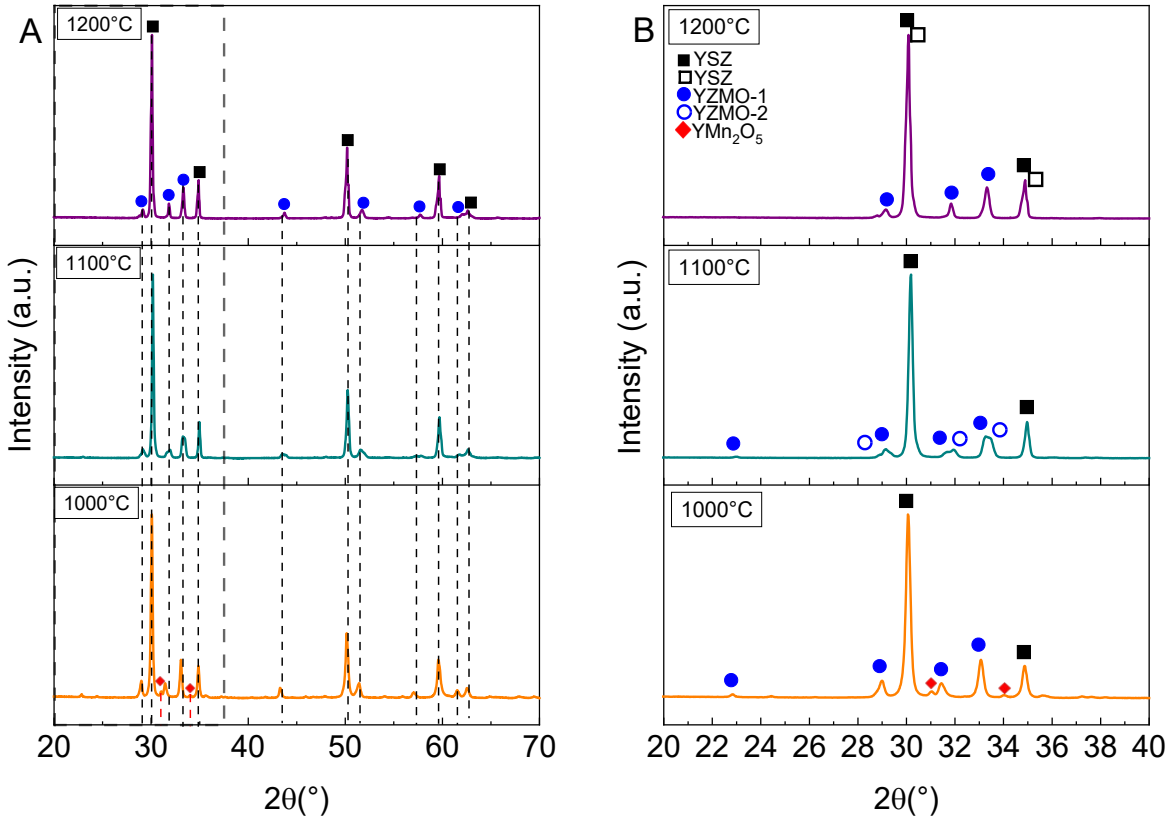

On the other hand, at 1100°C, the diffraction pattern reveals that the peaks located at 2θ=31.5 and 33º are doubled, suggesting the formation of two phases of the YZMO family with probably different Y^{3+}/Zr^{4+} ratio, a hypothesis that will be examined thereafter. In addition, according to previous works, and based on the comparison of XRD patterns, the second YZMO

(YZMO-2) phase exhibits a structure with a more symmetrical space group $P6_3/mmc$ vs $P6_3cm$ for the pristine material. In this more symmetrical crystalline structure, all the constitutive ions are located in parallel *ab* planes that facilitates the conduction of the O^{2-} anions (Moreno, 2018; Van Aken et al., 2004). Finally, T_2=1200°C, the $P6_3cm$-phase completely disappears so that only the $P6_3/mmc$-phase is observed, with a high Zr content(Moreno Botello et al., 2017, 2019; Moreno, 2018).

Figure 12.
X-ray diffraction pattern of A) $YMnO_3$ impregnated YSZ powder sintered at T_1=1300°C for different synthesis T_2 temperatures, B) zoom in the region 2θ=20°-40°.

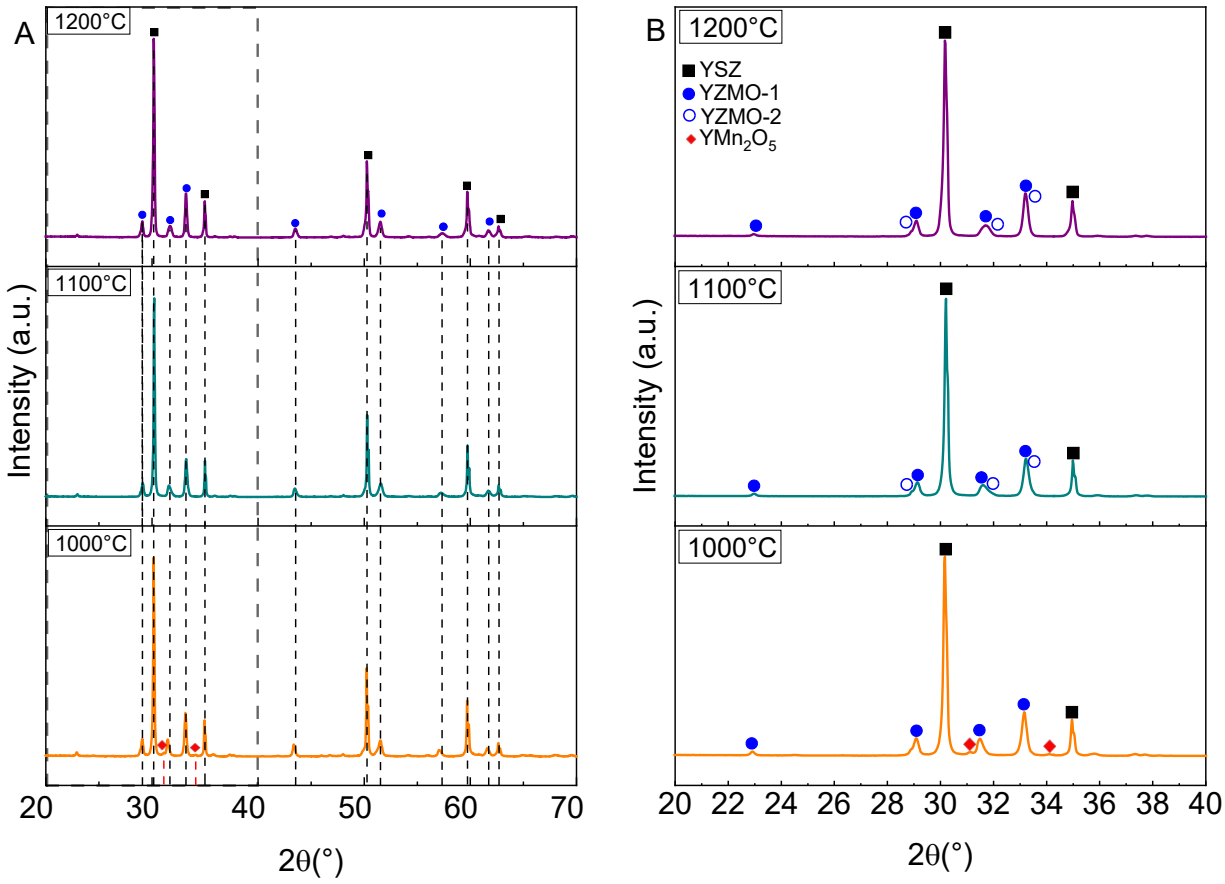

The diffraction patterns of the impregnated powder prepared at T_1=1300°C, after heat treatments of different T_2 are shown in Figure 12. The main difference observed by comparison

with Figure 11 is the presence of a $P6_3cm$-phase for T_2=1200°C, *i.e.* probably a lower content of Zr in the $YMnO_3$ phase that suggests a more difficult diffusion of Zr from YSZ to YMO due to the coarsening of the YSZ grains at the higher T_1 temperature.

Given that the synthesis method for the electrode is impregnation, the final product is shown to be not strictly the $YMnO_3$ phase (corresponding to the precursor solution): due to the reactivity with YSZ electrolyte, Zr cations migrated to the $YMnO_3$ structure resulting in a Zr-containing $YMnO_3$ phase, which composition is difficult to predict without a deeper analysis. In order to obtain information about the crystal structure of the different formed (Y,Zr)MnO_3 phases, the crystal structure of each phase was determined by refining the X-ray diffraction data with Rietveld method.

The results are summarized in Tables 3 and 4 for the scaffold sintered at T_1=1200°C and 1300°C, respectively (the graphical results are listed in Appendix C and D). In order to facilitate the comparison with the $P6_3/mmc$ crystalline structure, the $P6_3cm$ lattice parameters for the (Y,Zr)MnO_3 phase were also included. This comparison is possible since the parameters and the volume of the non-centrosymmetric and the centrosymmetric phases are related mathematically (see Appendix E) [53]. For T_1=1200°C, the synthesis temperature of T_2=1100°C promotes the formation of two YZMO phases with different lattice parameters and space group. A decrease in the cell parameters can be observed, that might be associated with a higher Zr concentration in the YZMO-2 phase than for YZMO-1 (the presence of Zr in $YMnO_3$ reduces its lattice parameters as Zr^{4+} is smaller than Y^{3+})(Van Aken et al., 2001). At a synthesis temperature of T_2=1200°C, the unique YZMO-1 phase exhibits smaller lattice parameters than for T_2=1100°C, again indicating a higher Zr^{4+} concentration. The increase of Zr content in YZMO is also reflected in the appearance

of a second YSZ phase (Rahaman, 2017) with different cell parameters from the YSZ initial matrix.

Table 3
Structural parameters of $YMnO_3$/YSZ sintered at T_1=1200°C, and synthesis at T_2=1100 and 1200°C, respectively, obtained from Rietveld refinement.

Synthesis Temperature T_2	Phase	Space group	a(Å)	c(Å)	V(Å^3)	Reliability factors
1100 °C	YSZ	*Fm-3m*	5.1405(2)	5.1405(2)	135.837(6)	R_p (%) = 5.33 GOF= 2.82 R_{wp} (%) = 7.14
	YZMO-1	*$P6_3cm$*	6.1469(6)	11.338(2)	371.03(1)	
	YZMO-2	*$P6_3/mmc$*	3.5305(5)	11.232(2)	121.257(8)	
		*$P6_3cm$**	6.1150	11.232(2)	363.771	
1200 °C	YSZ	*Fm-3m*	5.1343(4)	5.1343(4)	135.34(1)	R_p (%) = 6.11 GOF= 3.29 R_{wp} (%) = 8.21
	YZMO-1	*$P6_3/mmc$*	3.5323(4)	11.224(2)	121.28(1)	
		*$P6_3cm$**	6.1184	11.224(2)	363.84	
	YSZ*	*Fm-3m*	5.1491(6)	5.1491(6)	136.519(8)	

R_p: profile factor R_{wp}: weighted-profile factor GOF: goodness of fit
*Corresponding to the conversion of the space group (not calculated by Rietveld)

Table 4.
Structural parameters of $YMnO_3$/YSZ sintered at T_1=1300°C, and synthesis at T_2=1100 and 1200°C, respectively, obtained from Rietveld refinement.

Synthesis Temperature T_2	Phase	Space Group	a(Å)	c(Å)	V(Å^3)	Reliability factors
1100 °C	YSZ	*Fm-3m*	5.1394(2)	5.1394(2)	135.755(6)	R_p (%) = 7.18 GOF=4.11 R_{wp} (%) = 10.27
	YZMO-1	*P63cm*	6.1518(7)	11.351(2)	373.00(1)	
1200 °C	YSZ	*Fm-3m*	5.1387(3)	5.1387(3)	135.690(8)	R_p (%) = 7.38 GOF= 3.87 R_{wp} (%) = 9.84
	YZMO-1	*P63cm*	6.1533(8)	11.317(2)	371.09(2)	

R_p: profile factor R_{wp}: weighted-profile factor GOF: goodness of fit

For the powder sintered at T_1=1300°C, the synthesis temperature of T_2=1100°C leads to the formation of a YZMO-1 phase (Table 4), with higher lattice parameters than for the matrix pre-calcined at T_1=1200°C, meaning a lower concentration of Zr. The decrease of Zr content for the powder sintered at T_1=1300°C is probably related to the grain coarsening phenomenon as evidenced before (Figure 10), making both chemical reactivity and diffusion slower. Additionally, at a synthesis temperature of T_2=1200°C a YZMO-1 phase is observed that exhibits smaller cell parameters when compared to the 1100°C one, *i.e.* a higher Zr content. This result agrees with the higher atomic diffusion at a higher T_2 temperature.

Finally, to determine the Zr content in the different (Y,Zr)MnO_3 phases and considering the structural parameters displayed in Tables 3 and 4, a linear regression was performed using the available data of crystallographic cell volume as a function of Zr molar fraction in the Y site. The results were compared to the data published by Moreno *et al.*(Moreno, 2018) and Katsufuji *et al.* (Katsufuji et al., 2002) and organized in Table 5 and then plotted in Figure 13. In the case of the powder sintered at T_1=1200°C, the impregnated material obtained with a synthesis temperature of T_2=1100°C exhibits two different phases: a primary phase that corresponds to a Zr molar fraction of 0.030 on the Y site, accompanied by a secondary phase with a substantially higher Zr content of 0.255. In contrast, at T_2 = 1200 °C, the electrode shows a single manganite phase with a Zr molar fraction of 0.250. This value is notably higher than the maximum Zr incorporation reported by Moreno for a pure (Y,Zr)MnO_3 phase synthesized via the direct sol–gel method. Such an increased level of Zr substitution within the crystal lattice may contribute to enhanced oxygen-ion mobility, which could in turn improve the electrochemical performance of the material.(Moreno Botello et al., 2019)

Table 5

Cross-reference of structural parameters of $Y_xZr_{1-x}MnO_3$ (X= 0, 0.05, 0.1 and 0.20)

Reference	a(Å)	C(Å)	V(Å^3)	Synthesis technique
		X=0		
Moreno et al (2017)(Moreno, 2018)	6.1403(3)	11.3952(5)	372.08	Solid-state reaction
		X = 0.05		
Moreno et al (2017)(Moreno, 2018)	6.1398(3)	11.3619(6)	370.08	Solid-state reaction
		X = 0.1		
Moreno et al (2017)(Moreno, 2018)	6.1405(4)	11.3171(8)	368.46	Solid-state reaction
		X = 0.2		
Katsufuji et al (2002)(Katsufuji et al., 2002)	6.1258(5)	11.2407(6)	365.26	Solid-state reaction

Figure 13.

Linear regression between volume parameters of $Y_{1-x}Zr_xMnO_3$, for the YSZ/ $Y_{1-x}Zr_xMnO_3$ sintered at T_1=1200°C

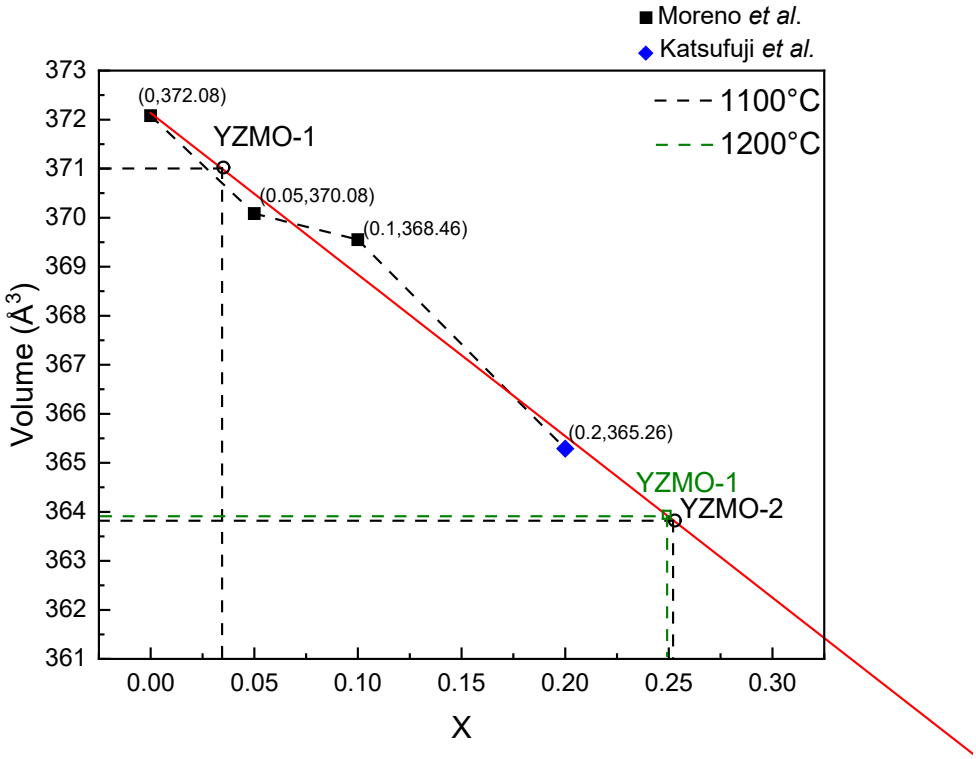

The effect of the coarsening phenomenon is manifested for a sintering temperature of YSZ powder at T_1=1300 °C. In this regard, there is no evidence of Zr diffusion at 1100°C as the cell parameters and volume of the manganite phase are the same as $YMnO_3$. In contrast, at 1200 °C, the material displays the same Zr molar fraction within the lattice as the main phase (YZMO-1) obtained from powder sintered at 1200 °C and synthesized at 1100 °C (Figure 14).

Figure 14

Linear regression between volume parameters of $Y_{1-x}Zr_xMnO_3$, for the YSZ/ $Y_{1-x}Zr_xMnO_3$ sintered at T_1=1300°C

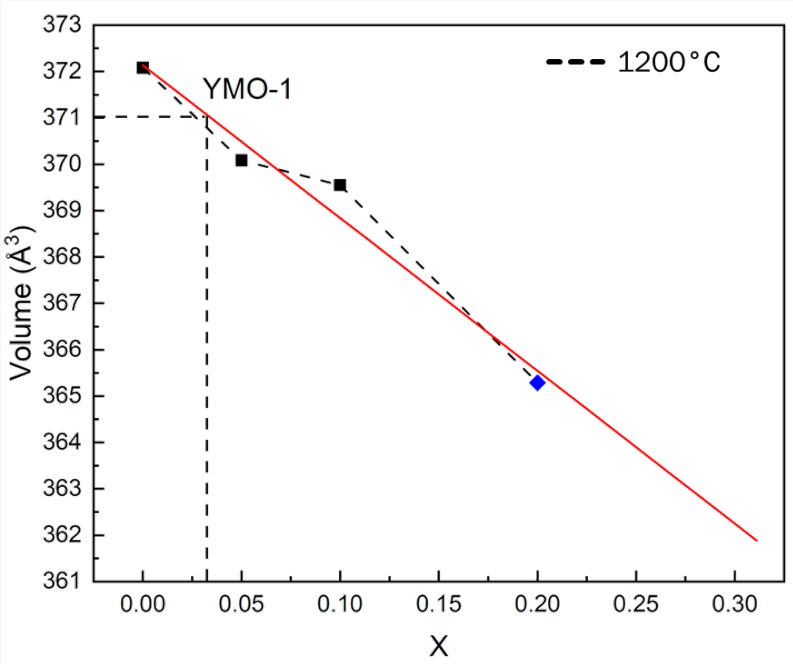

To further confirm the elemental distribution of YZMO-YSZ, transmission electron microscopy (TEM) and energy dispersive spectroscopy (EDS) were used for the characterization of the phases developed on YSZ sintered at T_1=1200°C. The elemental mapping of the material prepared at T_2=1100°C (Figure 15) confirmed the presence of Y, Zr and Mn in the grain composition. The major concentration of Mn and Zr in certain areas allowed to observe the difference between YSZ and YZMO grains. In the case of the elemental distribution of the powder

prepared at T_2=1200 °C (Figure 16), Y, Zr and Mn were homogeneously distributed in the entire grain, suggesting that the diffusion of Zr is well distributed through the grain.

Figure 15.
HAADF-EDS of the (Y,Zr)MnO_3/YSZ-1200°C powder after synthesis at T_2=1100°C for 3h.

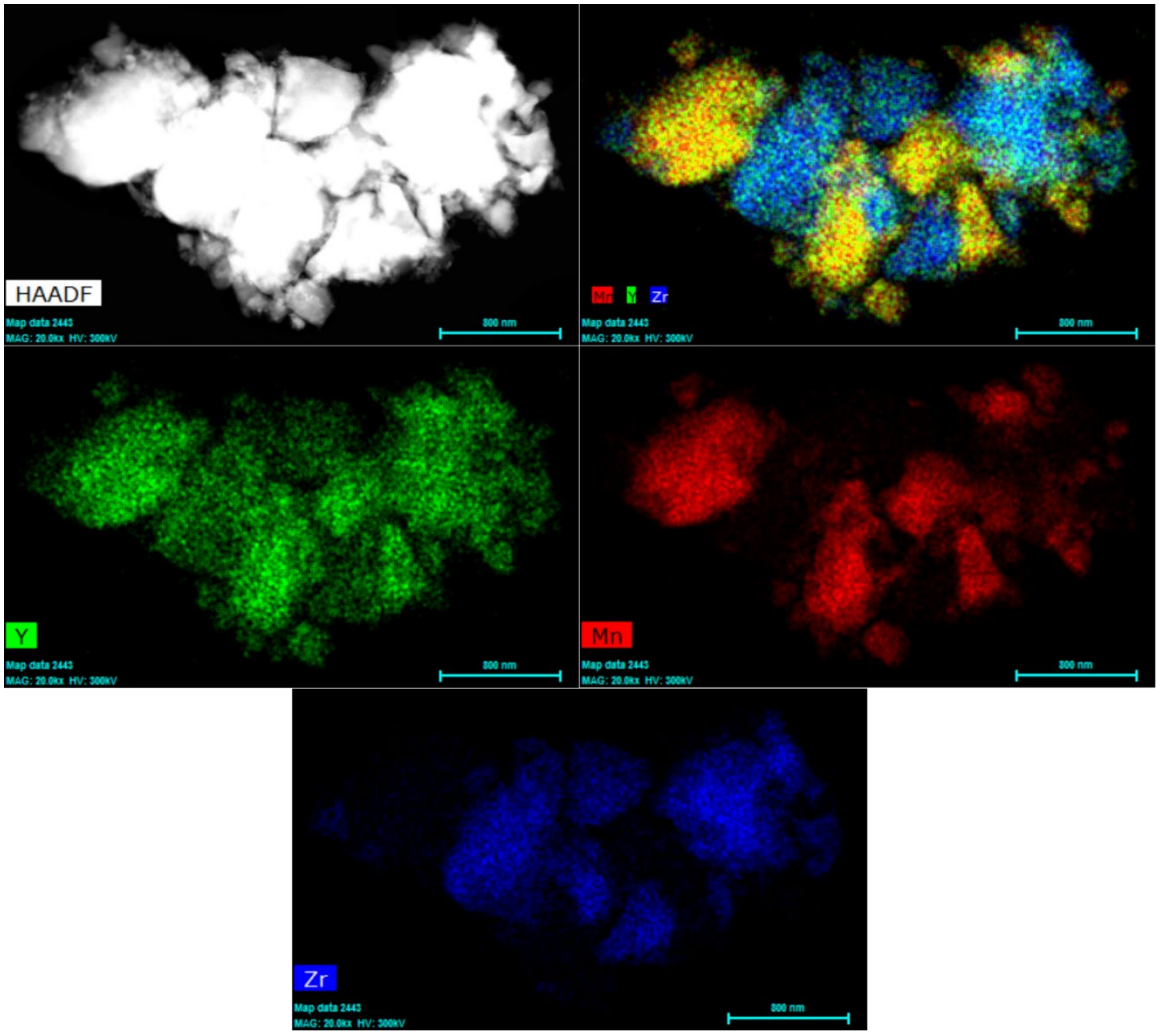

Figure 16

HAADF-EDS of the (Y,Zr)MnO_3/YSZ-1200°C powder after synthesis at T_2=1200°C for 3h.

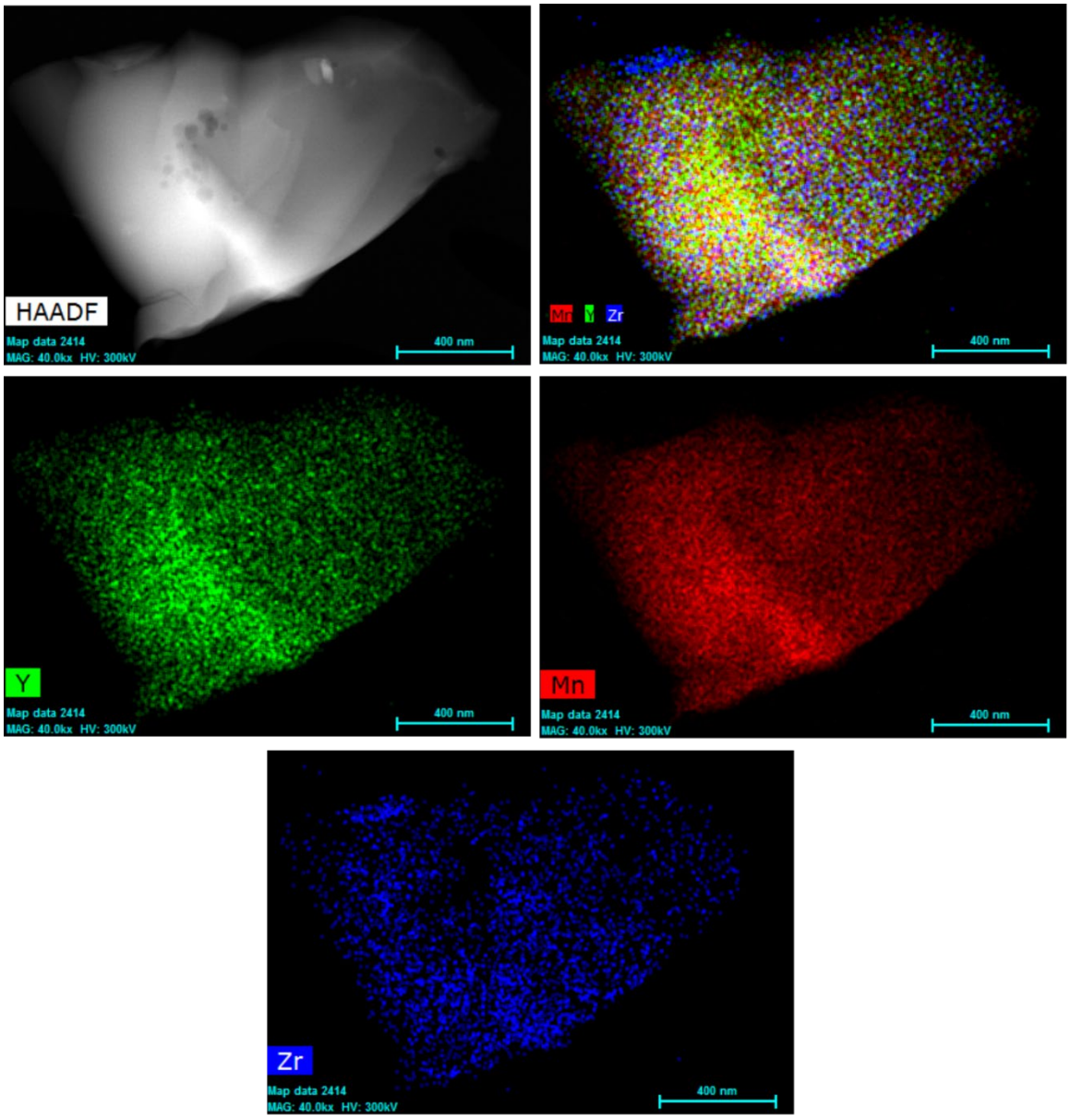

4.2 Scaffold Formation

A series of dense electrolytes were prepared by pressing commercial YSZ powder (YSZ-TC) with 2.5% PVA at 1 MPa for 2 min. The resulting dense YSZ pellets were calcinated at 700°C to remove PVA. Further, in agreement with the dilatometry analysis presented in Figure 17, they

were subsequently sintered at 1400 °C and finally polished using an MD-PIANO 220 disk and water as a lubricant (according to section 3.2.1), to achieve a uniform surface, reduce surface roughness and prepare them for the deposition of the YSZ scaffold by spray deposition.

Figure 17.
Dilatometry curve of commercial YSZ powder (YSZ-TC) from room temperature to 1600°C.

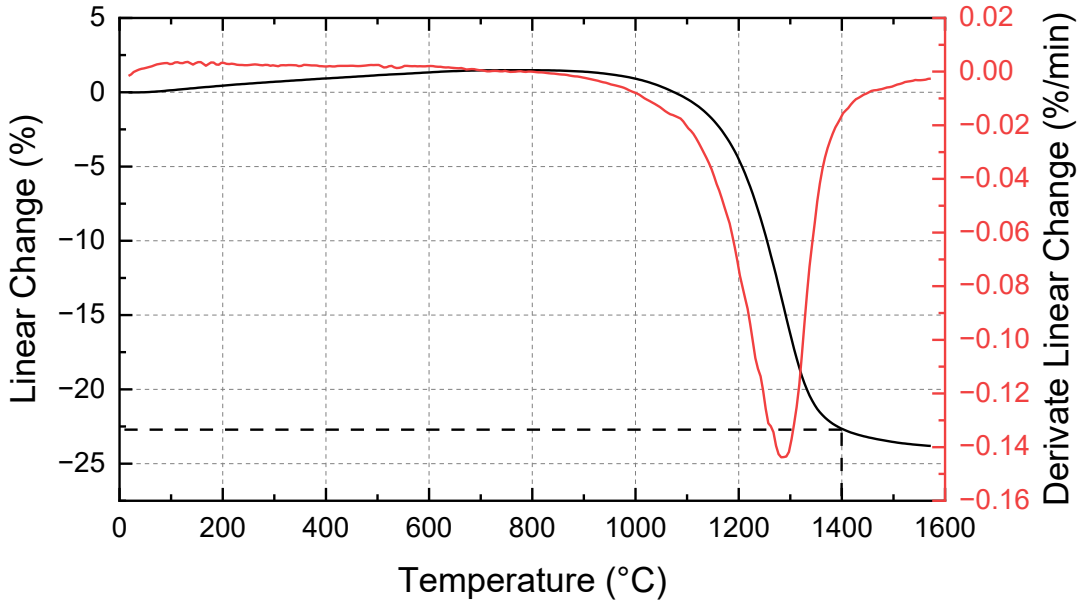

The analysis carried out through confocal microscopy (Figure 18-A) revealed that the surface of the sintered PSZ after polishing had a notable roughness difference of 19.74 µm and the grinding lines left by the disk were visible at a magnification of 280X.

Figure 18.
Surface of sintered YSZ pellet: A) Confocal micrograph at 280X and the 3D reconstruction; SEM micrograph: B) 400X and C)1600X.

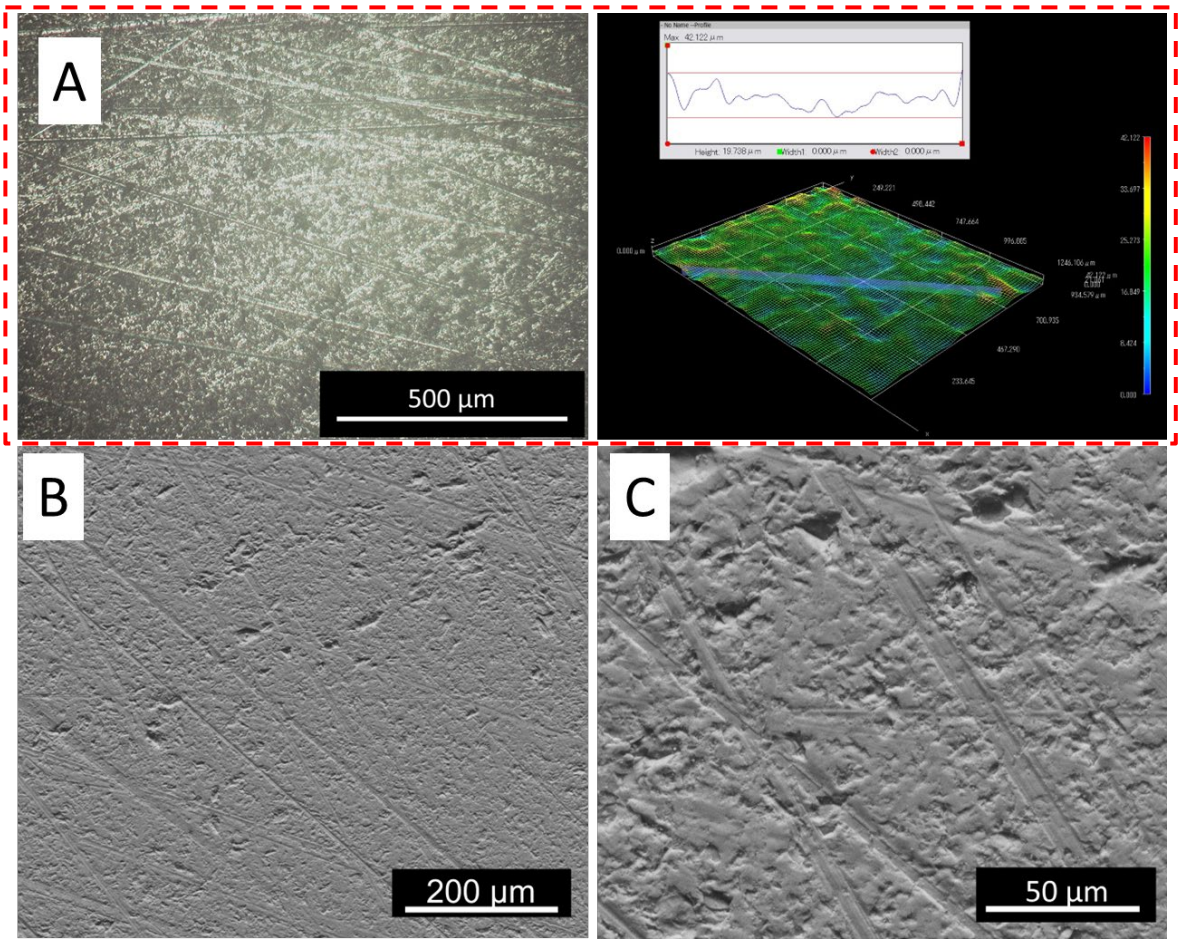

4.2.1 Preliminary study of deposition

The preliminary study of the process for deposition and formation of YSZ scaffold was performed with the aim to establish the role of some variables such as the use of fresh and 24 hours aged solution, as well as the deposition and sintering times.

Figure 19 shows surface micrographs of YSZ scaffolds after deposition and sintering of the two solutions. In Figure 19-A, the fresh solution produces uniform coating, although cracks are also visible. In contrast, in Figure 19-B the scaffold prepared with a solution aged for 24 hours

shows agglomerates of bigger sizes on the surface than the ones observed on the previous. These differences can be explained by colloidal stability. At very small particle sizes, van der Waals attractions become strong because of the high surface area, which promotes agglomeration. According to the Derjaguin–Landau–Verwey–Overbeek (DLVO) theory, the stability of the colloidal solution depends on the balance between the attraction and the electrostatic repulsion from the electrical double layer, when particles cross the repulsive barrier, they stick together permanently, forming aggregates(Göksel et al., 2024). The surface of the scaffold influences how uniformly the coating impregnates the substrate. Smoother scaffold surfaces (free of large random agglomerates) promote better wetting and spreading of the (Y,Zr)MnO3 precursors(Ma et al., 2025).

Figure 19

SEM image of scaffold sintered from a solution A) not aged B) aged for 24 h.

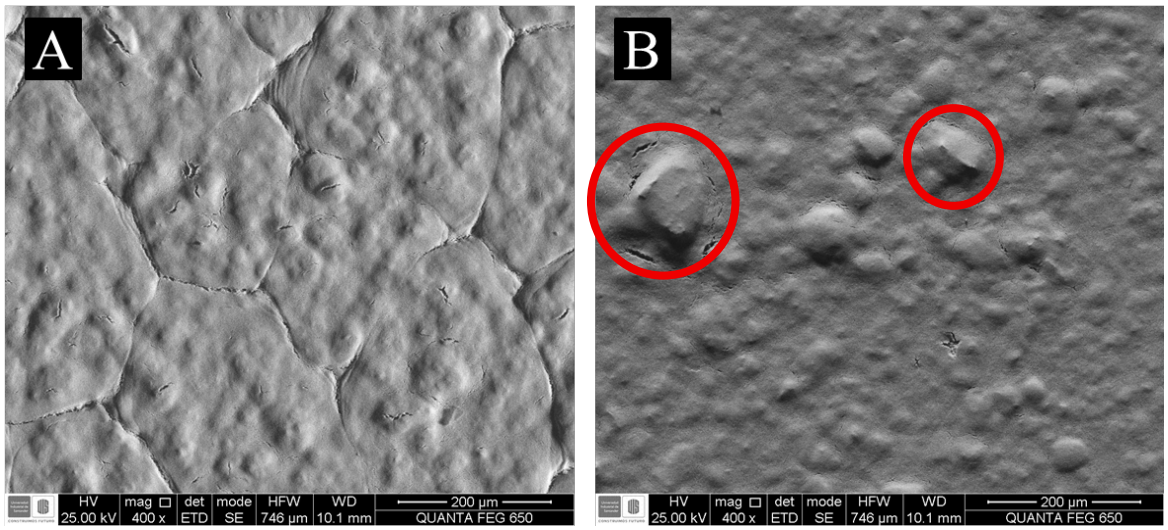

The influence of deposition time is shown in Figure 20. This parameter determines how much solution is deposited on the scaffold. With longer deposition times, the scaffold mass increases, but drying becomes uneven. As the solvent evaporates, solutes move toward the surface, creating a concentrated layer. This layer hardens into a crust, which prevents further shrinkage and builds

up internal stress. Larger droplets (Figure 19-D) are more likely to rupture because the pressure inside cannot be released once the crust has formed.(de Souza Lima et al., 2020).

Figure 20

Surface morphology of scaffolds sprayed at different deposition times of A) 2s, B) 3s, C) 4s, and D) 5s

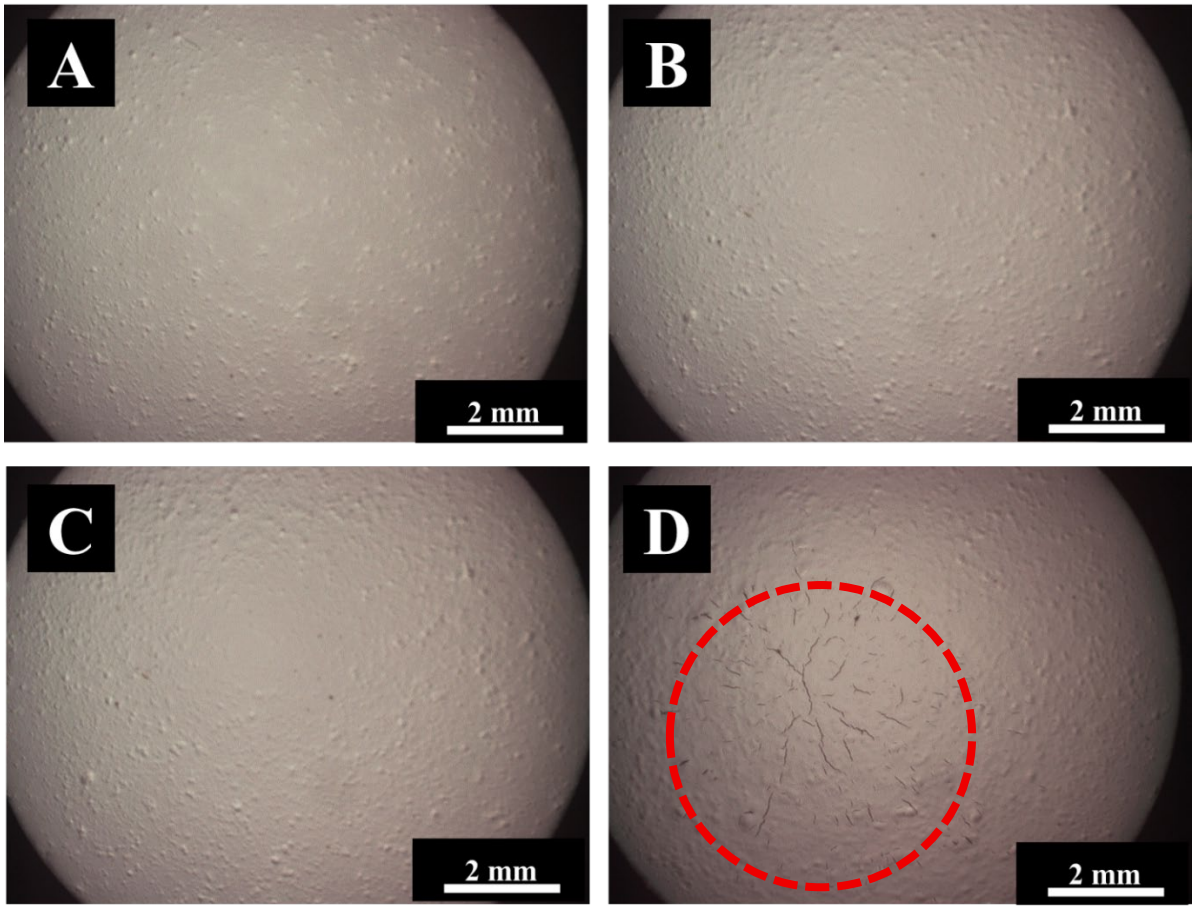

Lastly, the sintering time affects the microstructure and properties of the scaffold by augmenting the grain size of YSZ as time increases, causing a change in the grain size and grain boundaries, meaning that at the same temperature, but increasing the time spent on sintering might produce bigger grains well connected as seen in Figure 21, whereas shorter sintering times would produce finer grains with more limited connection(Song et al., 2018). In this regard, Figure 21-A shows the SEM micrograph of the cross-section of the scaffold sintered at T_1=1200 for 3h that presented

a granular microstructure, while the scaffold sintered for 24 h (Figure 21-B) exhibited a significant reduction in porosity due to increased grain sintering.An optimal sprayed scaffold features around 40–60% open porosity with a well-connected network of pores, a hierarchical pore size distribution (combining large channels for gas flow with smaller pores for high surface area), inherently rough and textured internal surfaces, and a high surface area available for catalyst deposition. Such characteristics ensure that the impregnating solution can penetrate and coat the scaffold uniformly, yielding a finely dispersed catalyst that greatly extends the triple-phase boundary and reaction sites.(Vohs & Gorte, 2009)

Figure 21

Effect of the sintering time of YSZ scaffold A) 1200 -3h B)1200 -24 h

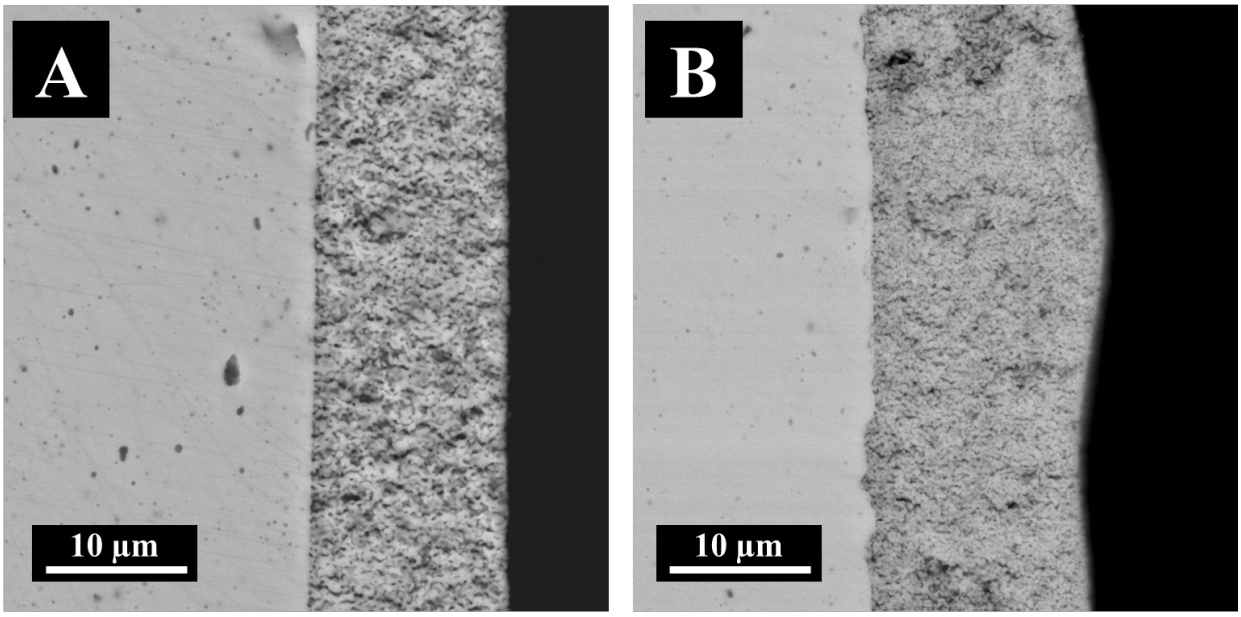

Based on the preliminary study, subsequent experiments will evaluate scaffold deposition followed by impregnation. Fresh solutions were selected in order to minimize surface defects observed with aged suspensions. A deposition time of 3 s was chosen since longer times promoted the formation of crack inside the scaffold. Nevertheless, the influence of the range of sintering times on the composition of the(Y,Zr)MnO_3 phase, since this parameter is expected to influence

pore filling and ultimately affect the composition and microstructural development of the impregnated.

4.2.2 Deposition of the porous electrolyte over the dense electrolyte

In this phase of the project, sintering time and temperature (T_1) were adjusted to observe the balance between grain interconnection and the porosity required for effective impregnation. Figures 22–23 illustrate that sintering time strongly influences the microstructure, with more pronounced changes observed between 3 and 6 h than between 12 and 24 h (Mosadeghkhah et al., 2007). The previous, since scaffold densification follows a logarithmic relation with sintering time, variations are more evident at short times and become less pronounced as sintering progresses. This behavior suggests that low temperatures combined with extended durations favor the development of scaffolds that retain good porosity while also forming well-developed grain necks.(Smart et al., 2013)

At 1200 °C, increasing the sintering time enhances grain-to-grain connectivity while simultaneously reducing scaffold porosity as a result of grain growth. After 3 h, the scaffold exhibits a granular morphology with limited contact between particles. By 12 h, individual grains are no longer clearly distinguishable, as grain boundaries merge and necks form between adjacent grains (Rahaman, 2017) . Extending the sintering duration to 24 h does not produce further significant modifications relative to the 12-h condition, indicating that the microstructural evolution approaches a plateau. This observation has practical implications, since prolonged sintering times increase energy consumption without contributing to additional improvements in scaffold quality (Mosadeghkhah et al., 2007; Song et al., 2018).

At 1300 °C, even at short sintering times, the scaffold exhibits lower porosity compared to samples treated at 1200 °C. After 3 hours, individual grains are no longer distinguishable, as grain

boundaries have merged and particles are interconnected through well-developed necks. Prolonging the sintering time further promotes grain growth, which results in increased densification and a corresponding reduction in scaffold porosity.

Figure 22

Effect of the sintering time at T_1=1200°C of YSZ scaffold at A) 3 h, B), 6 h, C) 12 h and D) 24 h.

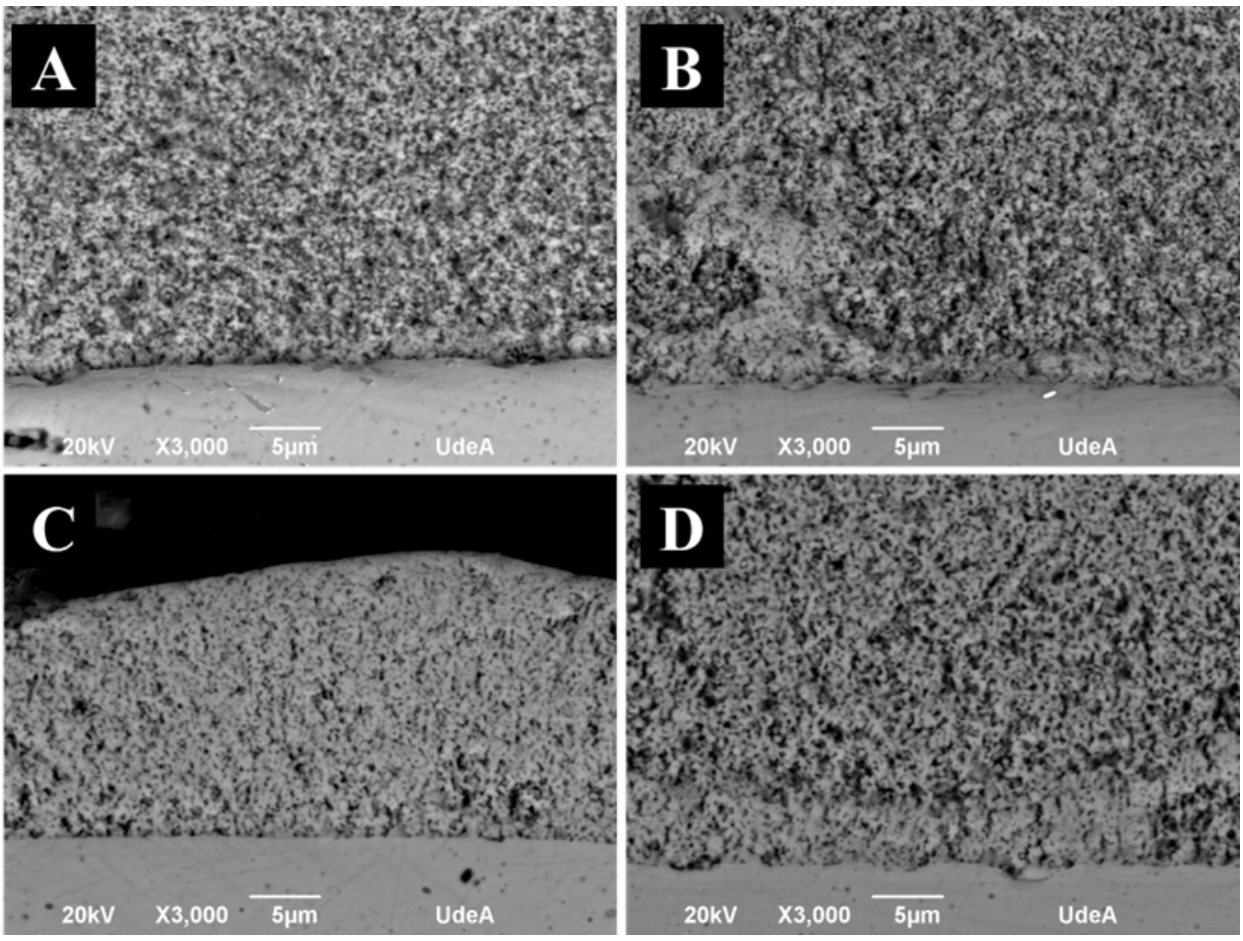

Figure 23

Effect of sintering time at T_1=1300°C of YSZ scaffold at A) 3 h, B), 6 h, C) 12 h and D) 24 h.

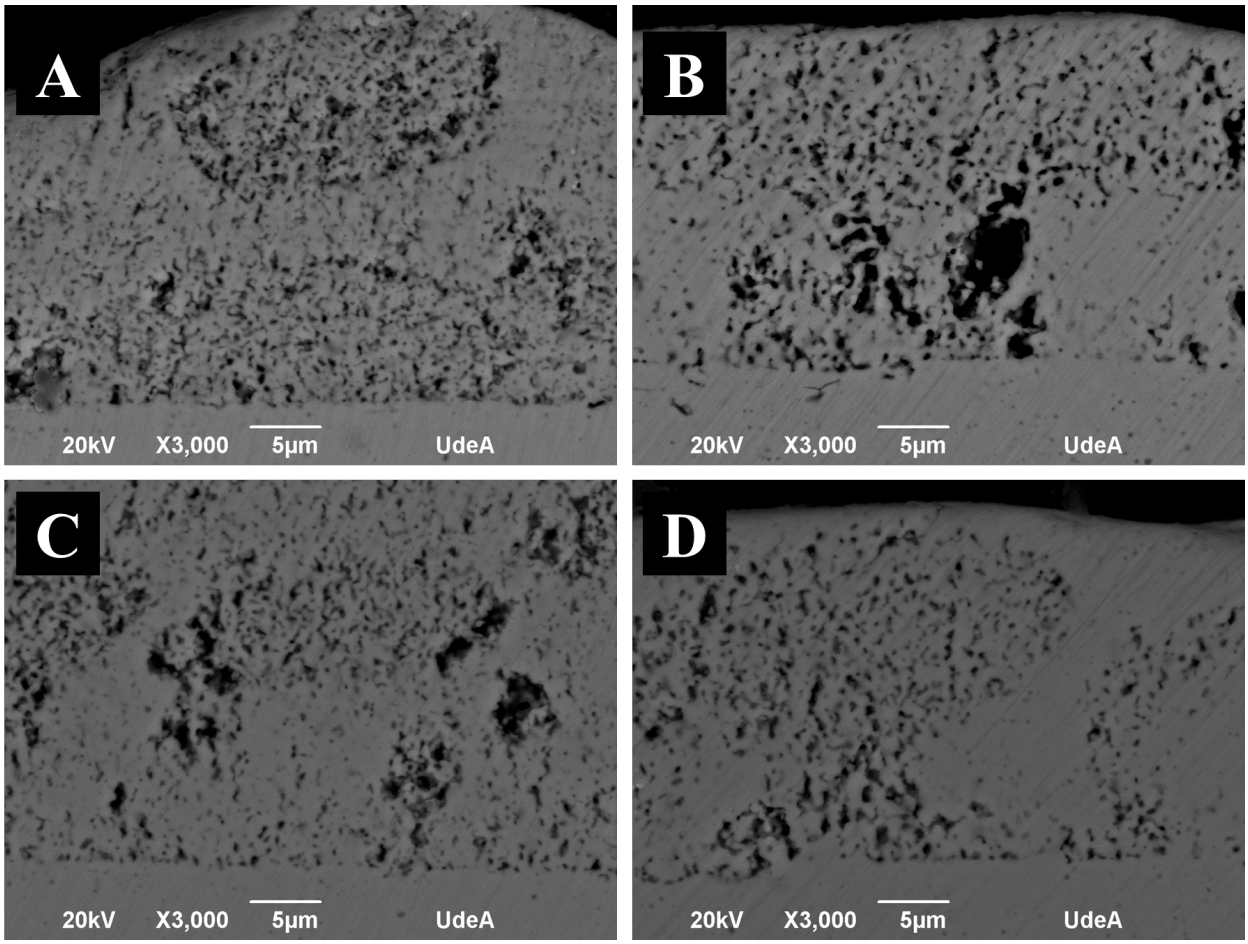

Following scaffold impregnation and cathode synthesis, Energy-Dispersive X-ray Spectroscopy (EDS) was employed to map the distribution of Mn within the structure. By contrasting the information derived from SEM analysis of the alteration in microstructure, it can be observed that Mn permeated into the structure, being the only element absent on the surface prior to impregnation. Furthermore, it is evident that most of the Mn is concentrated on the surface of the material. Across multiple cycles, most of the newly deposited material accumulates on the scaffold surface, because the pore architecture restricts deep penetration and the build-up of material in prior cycles narrows pathways. SEM-based image analysis confirms that infiltrated

phases predominantly coat accessible surfaces rather than distribute uniformly throughout the scaffold(Ni, n.d.).

Moreover, the difference between the capacity of impregnation between scaffold sintered at different temperatures is shown in figure 24-25, the EDS mapping representing T_1= 1200 °C shows a higher amount of permeation of Mn whereas the one representing T_1= 1300 °C have less quantities of Mn. This since higher temperatures increases the coarsening of the YSZ grain, thus reducing the porosity of the scaffold.

Figure 24.
EDS mapping of elemental Mn deposited via impregnation in YSZ scaffold sintered at T_1=1200°and synthesized at T_2= 1200°C with sintering time of A) 3 h, B) 6 h, C) 12 h and D) 24 h.

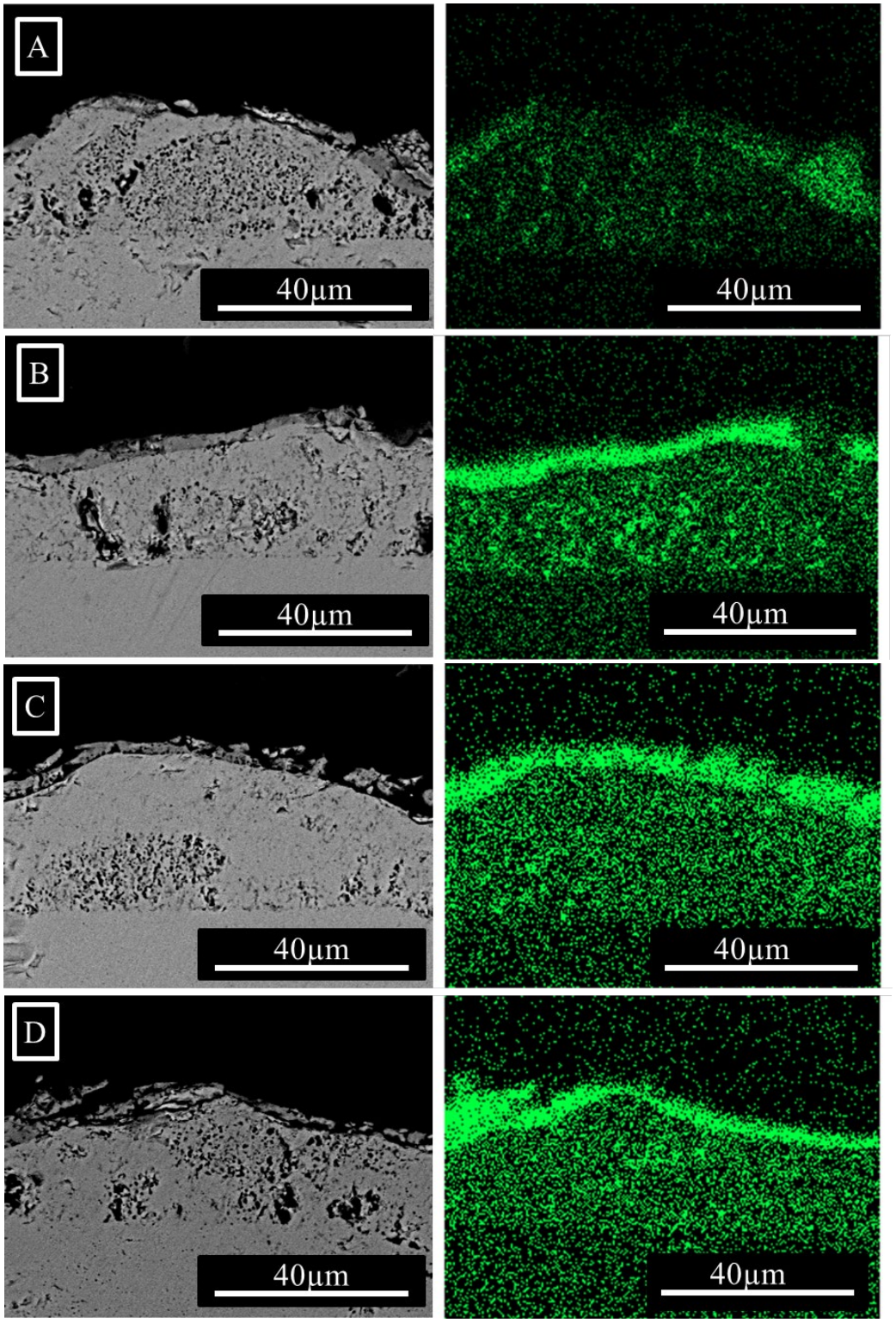

Figure 25.
EDS mapping of elemental Mn deposited via impregnation in YSZ scaffold sintered at T_1=1300°and synthesized at T_2= 1200°C with sintering time of A) 3 h, B) 6 h, C) 12 h and D) 24 h.

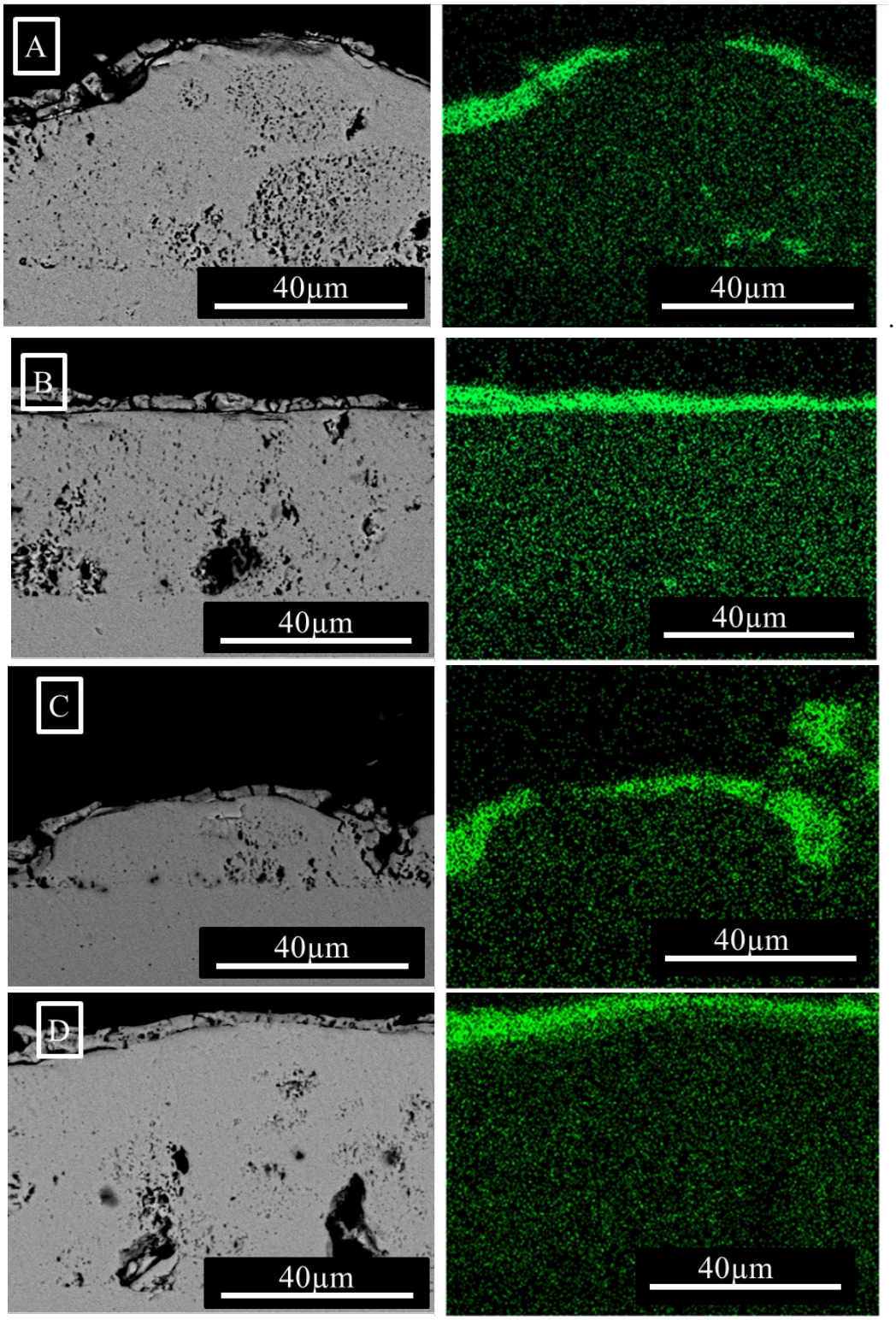

4.2.3 Synthesis of $YMnO_3$ on the scaffold

After establishing the scaffold sintering parameters, the next step was impregnation with a $YMnO_3$ precursor solution, using the optimal conditions identified in Chapter 1 (T_2 = 1200 °C for 3 h). Figure 26 presents the GIXRD patterns, that were collected at incidence angle of 2°, of the materials obtained after sintering at T_1 = 1200 °C for different durations (3, 6, 12, and 24 h) and subsequent synthesis. At t = 3 h (Figure 26A), no formation of the Zr-containing (Y,Zr)MnO_3 (YZMO-1) phase is detected on the YSZ scaffold. This scaffold exhibits larger pore sizes, which might allows the precursor solution to infiltrate deeper into the structure. As a result, the YZMO phase is distributed within the bulk rather than concentrated at the surface, leading to lower peak intensities in the diffraction pattern.

By contrast, at longer times (6, 12, and 24 h), the YZMO-1 phase becomes evident. The diffraction pattern (Figure 26B) reveals that the peak located at 2θ= 33º is doubled, suggesting the formation of two phases of the YZMO family with probably different Y^{3+}/Zr^{4+} ratio. In addition, according to previous works, and based on the comparison of XRD patterns, the second YZMO (YZMO-2) phase exhibits a structure with a more symmetrical space group P63/mmc vs P63cm for the pristine material.

Figure 26

X-ray diffraction pattern of $YMnO_3$ impregnated YSZ powder sintered at T_1=1200°C for different times, synthesized at 1200°C for 3 h, B) zoom in the region 2θ=20°-40°.

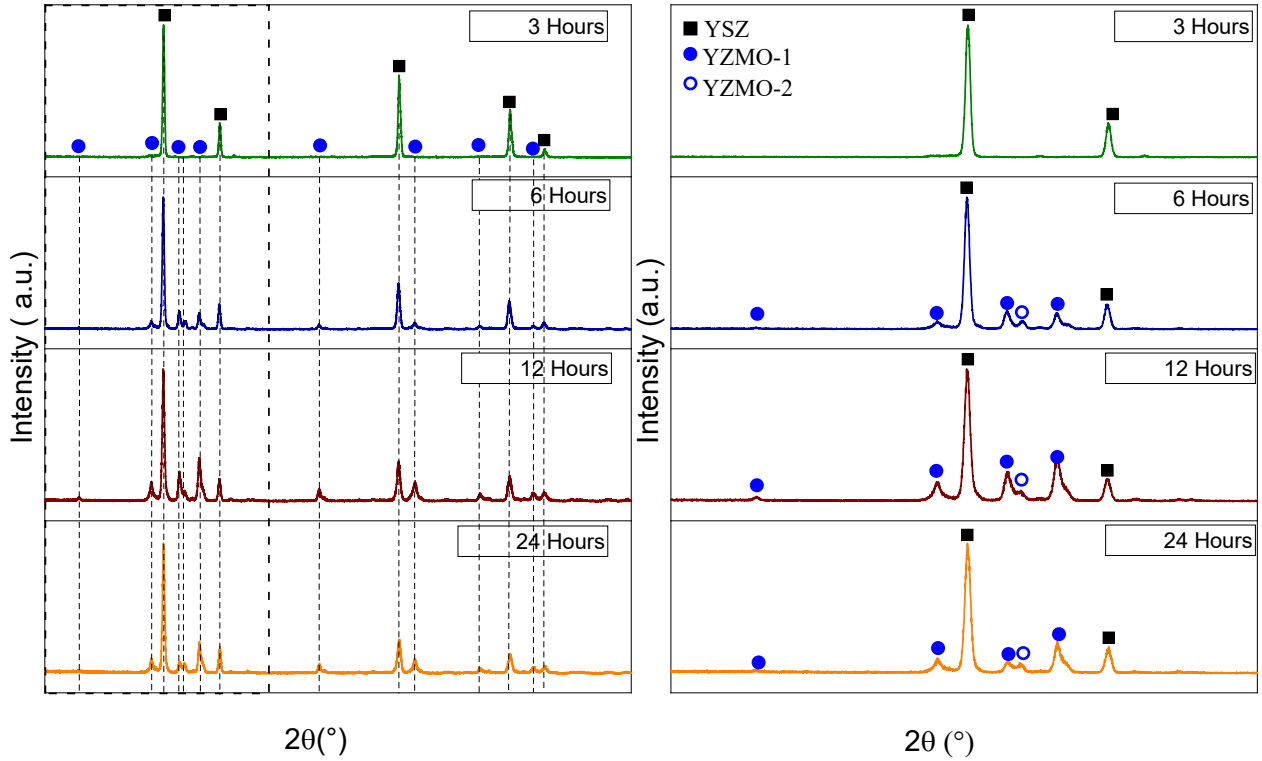

The results are summarized in Tables 6 for the scaffold sintered at T_1=1200°C. As previously mentioned, in order facilitate the comparison with the $P6_3/mmc$ crystalline structure, the $P6_3cm$ lattice parameters for the (Y,Zr)MnO_3 phase were also included. For t= 6, 12 and 24 h, the synthesis promotes the formation of two YZMO phases with different lattice parameters and space group. A decrease in the cell parameters can be observed, that might be associated with a higher Zr concentration in the YZMO-2 phase than for YZMO-1 (the presence of Zr in $YMnO_3$ reduces its lattice parameters as Zr^{4+} is smaller than Y^{3+})(Van Aken et al., 2001). At higher

sintering times the phase YZMO-2 exhibits a reduction cell volume parameter, again indicating a higher Zr^{4+} concentration.

Table 6

Structural parameters of YMnO3/YSZ sintered at T_1=1200°C at different sintering times, and synthesis at T_2=1200°C for 3h, obtained from Rietveld refinement.

Sintering Time	Phase	Space group	a(Å)	c(Å)	V(Å^3)	Reliability factors
6 Hours	YSZ	*Fm-3m*	5.1449(2)	5.1449(2)	136.2	Rp (%) = 16.69
	$YMnO_3$	*$P6_3cm$*	6.1410	11.3678	371.3	GOF= 1.09 Rwp (%) = 27.81
12 Hours	YSZ	*Fm-3m*	5.1445(2)	5.1445(2)	136.2	Rp (%) = 17.47
	YZMO-1	*$P6_3cm$*	6.1399(2)	11.3534(9)	370.8	GOF= 1.95
	YZMO-2	*$P6_3/mmc$*	3.5567(3)	11.2141(8)	122.9	Rwp (%) = 25.88
		*$P6_3cm$**	6.1613	11.2141	368.7	
24 Hours	YSZ	*Fm-3m*	5.1400(2)	5.1400 (2)	135.8	Rp (%) = 17.91
	YZMO-1	*$P6_3cm$*	6.1373 (2)	11.3489 (8)	370.2	GOF= 1.94
	YZMO-2	*$P6_3/mmc$*	3.5507(3)	11.2111(8)	122.4	Rwp (%) = 28.79
		*$P6_3cm$**	6.1499	11.2111	367.2	

Rp: profile factor Rwp: weighted-profile factor GOF: goodness of fit

Finally, the Zr content in the different (Y,Zr)MnO_3 phases was determined from the structural parameters listed in Table 6 using linear regression (Figure 27). For the scaffold sintered for 6 h at T_2 = 1200 °C, the impregnated material exhibits two phases: a primary phase with a Zr molar fraction of 0.025 on the Y site and a secondary phase with a markedly higher Zr content of 0.255. At 12 h, two manganite phases are again detected, with Zr molar fractions of 0.030 and

0.100. At 24 h, the material also shows two phases: the primary phase with a Zr molar fraction of 0.050 and the secondary phase with a higher Zr content of 0.140.

Figure 27
Linear regression between volume parameters of $Y_{1-x}Zr_xMnO_3$, for the YSZ/ $Y_{1-x}Zr_xMnO_3$ sintered at T_1=1200°C

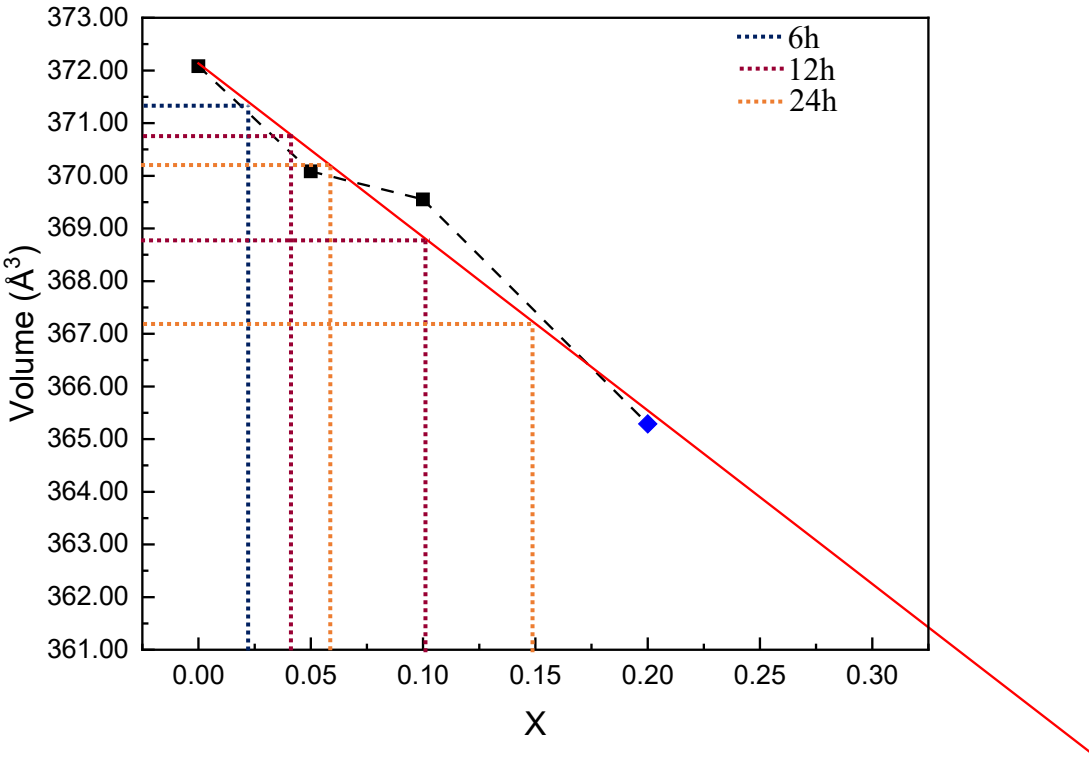

By increasing the sintering time, it is observed an increase in the amount of Zr diffusion from the scaffold to the YMnO3 grain. The latter being by the reduction of the pore size, the grain is in contact with more active area of the YSZ, on the other hand, by having larger pore sizes the contact area of the grain with the scaffold is diminished.

5. CONCLUSIONS

Compounds with stoichiometries $Y_{1-x}Zr_xMnO_3$ ($x < 0.255$) were successfully synthesized in both powder and scaffold forms using the incipient wet impregnation method. In both systems, Zr incorporation promoted a phase transition from the non-centrosymmetric $P6_3cm$ structure to the more symmetrical lamellar hexagonal $P6_3/mmc$ structure. However, Zr uptake was higher in the powder samples than in the scaffolds, as the latter provided fewer surface area to facilitate Zr diffusion from the electrolyte into the cathode.

Moreover, the change of phases shows that higher Zr dopping correlates with a change of the centrosymmetric $P6_3/mmc$ structure, which enhances oxygen ion conduction. However, the extent of this structural transition depends on the scaffold microstructure: finer, more porous scaffolds obtained at lower sintering temperatures (T_1) and moderate sintering times promote deeper Zr diffusion and a more homogeneous distribution of (Y,Zr)MnO_3 phases, whereas denser scaffolds restrict the diffusion of Zr to the cathode.

As a final point of this work, the effect of sintering time and synthesis time on scaffold formation must be considered. Consistent with the previous work, both the sintering and synthesis temperatures of 1200 °C were found to be optimal for achieving higher Zr incorporation. Under these conditions, the coarsening of the scaffold is driven by the temperature as well as the sintering and synthesis durations, which directly influence grain growth and hence the overall size and connectivity of the scaffold microstructure increase, further reducing the porosity.

6. RECOMMENDATIONS

For the study of the stability of the scaffold solution it is recommended that the conditions of aging can be maintained at different times, evaluating the change in the viscosity of the solution and the microscopy of the surface of the scaffold after being sintered in comparison with those worked in this thesis in order to evaluate the effectiveness of viscosity on the surface development.

Additionally, it is recommended to optimize the scaffold porosity in order to determine the effect of the previous solution, and if it is rather necessary the addition of porous makers (graphite) to the solution. Moreover, once the scaffold its optimized evaluate the cathode electrochemical performance with a deep study of the pO_2 dependence on the EIS measurement, the previous with the data of Moreno (in-situ vs ex-situ cathode preparation), will probably help to determine the attribution made by Moreno that the performance is subject to their microstructural characteristics.

REFERENCES

Batool, M., Sattar, M., Barki, U. K., & Khan, Z. S. (2018). Synthesis of Ni/YSZ based anode and investigation of effect of PVA as pore-former upon porosity, microstructure and thermal behavior for potential use in solid oxide fuel cells (SOFCs). *International Journal of Materials Research*, *109*(12), 1153–1159. https://doi.org/10.3139/146.111713

Bernardo, V. B. V., & Vert Belenguer, V. (2011). ELECTRODOS AVANZADOS PARA PILAS DE COMBUSTIBLE DE ÓXIDO SÓLIDO (SOFCs). *Tesis Doctoral*, (Universidad Politécnica de Valencia, Valencia, España.), 31–32.

Bezemer, G. L., Bitter, J. H., Kuipers, H. P. C. E., Oosterbeek, H., Holewijn, J. E., Xu, X., Kapteijn, F., Van Diilen, A. J., & De Jong, K. P. (2006). Cobalt particle size effects in the Fischer-Tropsch reaction studied with carbon nanofiber supported catalysts. *Journal of the American Chemical Society*, *128*(12), 3956–3964. https://doi.org/10.1021/ja058282w

Chen, Y., Zhou, W., Ding, D., Liu, M., Ciucci, F., Tade, M., & Shao, Z. (2015). Advances in Cathode Materials for Solid Oxide Fuel Cells: Complex Oxides without Alkaline Earth Metal Elements. *Advanced Energy Materials*, *5*(18), 1–34. https://doi.org/10.1002/aenm.201500537

de Souza Lima, R., Ré, M. I., & Arlabosse, P. (2020). Drying droplet as a template for solid formation: A review. In *Powder Technology* (Vol. 359, pp. 161–171). Elsevier B.V. https://doi.org/10.1016/j.powtec.2019.09.052

Doleker, K. M., Ozgurluk, Y., & Karaoglanli, A. C. (2018). Isothermal oxidation and thermal cyclic behaviors of YSZ and double-layered YSZ/La2Zr2O7 thermal barrier coatings

(TBCs). *Surface and Coatings Technology*, *351*(July), 78–88. https://doi.org/10.1016/j.surfcoat.2018.07.069

Duan, Z., Yang, M., Yan, A., Hou, Z., Dong, Y., Chong, Y., Cheng, M., & Yang, W. (2006a). Ba0.5Sr0.5Co0.8Fe0.2O3- δ as a cathode for IT-SOFCs with a GDC interlayer. *Journal of Power Sources*, *160*(1), 57–64. https://doi.org/10.1016/j.jpowsour.2006.01.092

Duan, Z., Yang, M., Yan, A., Hou, Z., Dong, Y., Chong, Y., Cheng, M., & Yang, W. (2006b). Ba0.5Sr0.5Co0.8Fe0.2O3−δ as a cathode for IT-SOFCs with a GDC interlayer. *Journal of Power Sources*, *160*(1), 57–64. https://doi.org/10.1016/j.jpowsour.2006.01.092

Energy and Environmental Solutions. (2000). Fuel Cell Handbook, Fifth Edition. In *Phytochemistry* (Vol. 26, Number 4). https://doi.org/10.2172/769283

Fan, L., Zhu, B., Su, P. C., & He, C. (2018). Nanomaterials and technologies for low temperature solid oxide fuel cells: Recent advances, challenges and opportunities. *Nano Energy*, *45*(December), 148–176. https://doi.org/10.1016/j.nanoen.2017.12.044

Gao, Y., Wu, Y. J., Chen, X. M., Cheng, J. P., Lin, Y. Q., & Ma, Y. (2008). Dense YMn2O5 ceramics prepared by spark plasma sintering. *Journal of the American Ceramic Society*, *91*(11), 3728–3730. https://doi.org/10.1111/j.1551-2916.2008.02671.x

Göksel, B., Koos, E., Vleugels, J., & Braem, A. (2024). Optimizing dispersants for direct ink writing of alumina toughened zirconia (ATZ) ceramics: Insights into suspension behavior and rheological properties. *Ceramics International*, *50*(19), 37010–37022. https://doi.org/10.1016/j.ceramint.2024.07.090

Ishihara, Tatsumi. (2009). *Perovskite Oxide for Solid Oxide Fuel Cells* (T. Ishihara, Ed.). Springer US. https://doi.org/10.1007/978-0-387-77708-5

Jian, G., Xu, Y., Lai, L. C., Wang, C., & Zachariah, M. R. (2014). Mn3O4 hollow spheres for lithium-ion batteries with high rate and capacity. *Journal of Materials Chemistry A*, *2*(13), 4627–4632. https://doi.org/10.1039/c4ta00207e

Jiang, S. P. (2006a). A review of wet impregnation - An alternative method for the fabrication of high performance and nano-structured electrodes of solid oxide fuel cells. *Materials Science and Engineering A*, *418*(1–2), 199–210. https://doi.org/10.1016/j.msea.2005.11.052

Jiang, S. P. (2006b). A review of wet impregnation—An alternative method for the fabrication of high performance and nano-structured electrodes of solid oxide fuel cells. *Materials Science and Engineering: A*, *418*(1–2), 199–210. https://doi.org/10.1016/j.msea.2005.11.052

Katsufuji, T., Masaki, M., Machida, A., Moritomo, M., Kato, K., Nishibori, E., Takata, M., Sakata, M., Ohoyama, K., Kitazawa, K., & Takagi, H. (2002). Crystal structure and magnetic properties of hexagonal RMnO3 (R =Y, Lu, and Sc) and the effect of doping. *Physical Review B*, *66*(13), 134434. https://doi.org/10.1103/PhysRevB.66.134434

Kawada, T. (2009). Perovskite Oxide for Cathode of SOFCs. In *Perovskite Oxide for Solid Oxide Fuel Cells* (pp. 147–166). https://doi.org/10.1007/978-0-387-77708-5_7

Kim, J., Seo, W. Y., Shin, J., Liu, M., & Kim, G. (2013). Composite cathodes composed of NdBa0.5Sr0.5Co 2O5+δ and Ce0.9Gd0.1O 1.95 for intermediate-temperature solid oxide fuel cells. *Journal of Materials Chemistry A*, *1*(3), 515–519. https://doi.org/10.1039/c2ta00025c

Ma, L., Ma, Y., Yu, K., Xu, H., Hao, J., Li, Y., Wang, K., & Sun, D. (2025). The Effect of Substrate Roughness and Impact Angle on Droplet Spreading in Spraying. *Coatings*, *15*(2). https://doi.org/10.3390/coatings15020242

Mahato, N., Banerjee, A., Gupta, A., Omar, S., & Balani, K. (2015). Progress in material selection for solid oxide fuel cell technology: A review. *Progress in Materials Science*, *72*, 141–337. https://doi.org/10.1016/j.pmatsci.2015.01.001

Mekhilef, S., Saidur, R., & Safari, A. (2012). Comparative study of different fuel cell technologies. *Renewable and Sustainable Energy Reviews*, *16*(1), 981–989. https://doi.org/10.1016/j.rser.2011.09.020

Minh, N. Q., & Takahashi, T. (1995a). Cathode. In *Science and Technology of Ceramic Fuel Cells* (Number iii, pp. 117–146). Elsevier. https://doi.org/10.1016/b978-044489568-4/50006-2

Minh, N. Q., & Takahashi, T. (1995b). Electrical conduction in ceramics. *Science and Technology of Ceramic Fuel Cells*, (i), 41–68. https://doi.org/10.1016/b978-044489568-4/50004-9

Minh, N. Q., & Takahashi, T. (1995c). Electrode Reaction. In *Science and Technology of Ceramic Fuel Cells* (Vol. 26, p. 366). Elsevier. https://doi.org/10.1016/B978-044489568-4/50009-8

Minh, N. Q., & Takahashi, T. (1995d). Introduction. *Science and Technology of Ceramic Fuel Cells*, (iii), 1–14. https://doi.org/10.1016/b978-044489568-4/50002-5

Mitterdorfer, A., & Gauckler, L. J. (1998). La2Zr2O7 formation and oxygen reduction kinetics of the La0.85Sr0.15MnyO3, O2(g)|YSZ system. *Solid State Ionics*, *111*(3–4), 185–218. https://doi.org/10.1016/s0167-2738(98)00195-7

Mizusaki, J., Yonemura, Y., Kamata, H., Ohyama, K., Mori, N., Takai, H., Tagawa, H., Dokiya, M., Naraya, K., Sasamoto, T., Inaba, H., & Hashimoto, T. (2000). Electronic conductivity, Seebeck coefficient, defect and electronic structure of nonstoichiometric La1-xSrxMnO3. *Solid State Ionics*, *132*(3), 167–180. https://doi.org/10.1016/s0167-2738(00)00662-7

Moreno Botello, Z. L., Caneiro, A., Roussel, P., & Gauthier, G. (2017). Synthesis and preliminary study of pure and Zr-doped YMnO3compounds as Solid Oxide Fuel Cells electrode. *Journal of Alloys and Compounds*, *690*, 348–355. https://doi.org/10.1016/j.jallcom.2016.08.125

Moreno Botello, Z. L., Montenegro, A., Grimaldos Osorio, N., Huvé, M., Pirovano, C., Småbråten, D. R., Selbach, S. M., Caneiro, A., Roussel, P., & Gauthier, G. H. (2019). Pure and Zr-doped YMnO3+δ as a YSZ-compatible SOFC cathode: a combined computational and experimental approach. *Journal of Materials Chemistry A*, *7*(31), 18589–18602. https://doi.org/10.1039/C9TA04912F

Moreno, Z. (2018). *STUDY OF MATERIALS DERIVED FROM YMNO3-MANGANITE AS SOFC ELECTRODES*. Universidad Industrial de Santander.

Mosadeghkhah, A., Alaee, M. A., & Mohammadi, T. (2007). Effect of sintering temperature and dwell time and pressing pressure on Ba0.5Sr0.5Co0.8Fe0.2O3- δ perovskite-type membranes. *Materials and Design*, *28*(5), 1699–1706. https://doi.org/10.1016/j.matdes.2006.03.007

Mudinepalli, V. R., Song, S., & Murty, B. S. (2013). Microwave sintering effect on structural and dielectrical properties of Ba1-x(Sr/Pb)xTiO3 (x = 0.2 for Sr and Pb) ceramics. *Journal of Materials Science: Materials in Electronics*, *24*(6), 2141–2150. https://doi.org/10.1007/s10854-013-1072-y

Ni, C. (n.d.). *OPTIMISATION AND TESTING OF LARGE CERAMIC-IMPREGNATED SOLID OXIDE FUEL CELLS (SOFCS)*. Retrieved http://research-repository.st-andrews.ac.uk/

Noda, Y., Kimura, H., Kamada, Y., Osawa, T., Fukuda, Y., Ishikawa, Y., Kobayashi, S., Wakabayashi, Y., Sawa, H., Ikeda, N., & Kohn, K. (2006). Relation between ferroelectric

and antiferromagnetic order in RMn2 O5. *Physica B: Condensed Matter*, *385-386 I*, 119–122. https://doi.org/10.1016/j.physb.2006.05.179

Osinkin, D. A., Bogdanovich, N. M., Beresnev, S. M., & Zhuravlev, V. D. (2015). High-performance anode-supported solid oxide fuel cell with impregnated electrodes. *Journal of Power Sources*, *288*, 20–25. https://doi.org/10.1016/j.jpowsour.2015.04.098

Palakkathodi Kammampata, S. (2014). *Porous Yttria-Stabilized Zirconia Microstructures for SOFC Anode Fabrication*. UNIVERSITY OF CALGARY.

Parajón-Costa, B. S., Wagner, C. C., & Baran, E. J. (2003). Fuel cell handook. *Zeitschrift Für Anorganische Und Allgemeine Chemie*, *629*(6), 1085–1090. https://doi.org/10.1002/zaac.200300050

Petříček, V., Dušek, M., & Palatinus, L. (2014). Crystallographic Computing System JANA2006: General features. *Zeitschrift Für Kristallographie - Crystalline Materials*, *229*(5), 345–352. https://doi.org/10.1515/zkri-2014-1737

Rahaman, M. N. (2017). Ceramic processing and sintering, second edition. In *Ceramic Processing and Sintering, Second Edition*. CRC Press. https://doi.org/10.1201/9781315274126

Sandoval, M., Caldes, M. T., Mogni, L., At, C., Examinateurs, C., Ni, M. E., Alirio, F., Directeurs, S., Co-encadrante, P. R., & Rapporteurs, C. P. (2017). *Etude des manganites Ruddlesden-Popper RE x A 2-x MnO 4 (RE : La , Nd et A : Sr , Ca) en vue de leur application en tant que matériaux d ′ électrode de pile à combustible à oxide solide (SOFC) Study of Ruddlesden-Popper manganites RE x A 2-x MnO 4 (R. 4*.

Setevich, C., Larrondo, S., & Prado, F. (2018). Infiltrated La0.5Ba0.5CoO3-δ in La0.8Sr0.2Ga0.8Mg0.2O2.8 scaffolds as cathode material for IT-SOFC. *Ceramics International*, *44*(14), 16851–16858. https://doi.org/10.1016/j.ceramint.2018.06.121

Shen, F., & Lu, K. (2015). Comparative study of La0.6Sr0.4Co0.2Fe0.8O3, Ba0.5Sr0.5Co0.2Fe0.8O3 and Sm0.5Sr0.5Co0.2Fe0.8O3 cathodes and the effect of Sm0.2Ce0.8O2 block layer in solid oxide fuel cells. *International Journal of Hydrogen Energy*, *40*(46), 16457–16465. https://doi.org/10.1016/j.ijhydene.2015.09.148

Shen, F., & Lu, K. (2016). Perovskite-type La0.6Sr0.4Co0.2Fe0.8O3, Ba0.5Sr0.5Co0.2Fe0.8O3, and Sm0.5Sr0.5Co0.2Fe0.8O3 cathode materials and their chromium poisoning for solid oxide fuel cells. *Electrochimica Acta*, *211*, 445–452. https://doi.org/10.1016/j.electacta.2016.06.070

Sholklapper, T. Z., Kurokawa, H., Jacobson, C. P., Visco, S. J., & De Jonghe, L. C. (2007). Nanostructured Solid Oxide Fuel Cell Electrodes. *Nano Letters*, *7*(7), 2136–2141. https://doi.org/10.1021/nl071007i

Singhal, S. C., & Kendall, K. (2003). Introduction to SOFCs. In *High-temperature Solid Oxide Fuel Cells: Fundamentals, Design and Applications*. Elsevier Ltd. https://doi.org/10.1016/B978-185617387-2/50018-0

Smart, S., Liu, S., Serra, J. M., Diniz da Costa, J. C., Iulianelli, A., & Basile, A. (2013). Porous ceramic membranes for membrane reactors. In *Handbook of Membrane Reactors* (Vol. 1, pp. 298–336). Elsevier Inc. https://doi.org/10.1533/9780857097330.2.298

Song, B., Ruiz-Trejo, E., & Brandon, N. P. (2018). Enhanced mechanical stability of Ni-YSZ scaffold demonstrated by nanoindentation and Electrochemical Impedance Spectroscopy.

Journal of Power Sources, *395*(May), 205–211. https://doi.org/10.1016/j.jpowsour.2018.05.075

Stochniol, G., Syskakis, E., & Naoumidis, A. (1995). Chemical Compatibility between Strontium-Doped Lanthanum Manganite and Yttria-Stabilized Zirconia. *Journal of the American Ceramic Society*, *78*(4), 929–932. https://doi.org/10.1111/j.1151-2916.1995.tb08416.x

Sun, C., Hui, R., & Roller, J. (2010). Cathode materials for solid oxide fuel cells: A review. *Journal of Solid State Electrochemistry*, *14*(7), 1125–1144. https://doi.org/10.1007/s10008-009-0932-0

Tarasi, F., Alebrahim, E., Dolatabadi, A., & Moreau, C. (2019). A Comparative study of YSZ suspensions and coatings. *Coatings*, *9*(3). https://doi.org/10.3390/COATINGS9030188

Tu, H., & Stimming, U. (2004). Advances, aging mechanisms and lifetime in solid-oxide fuel cells. *Journal of Power Sources*, *127*(1–2), 284–293. https://doi.org/10.1016/j.jpowsour.2003.09.025

Van Aken, B. B., Bos, J.-W. G., de Groot, R. A., & Palstra, T. T. M. (2001). Asymmetry of electron and hole doping in YMnO3. *Physical Review B*, *63*(12), 125127. https://doi.org/10.1103/PhysRevB.63.125127

Van Aken, B. B., Palstra, T. T. M., Filippetti, A., & Spaldin, N. A. (2004). The origin of ferroelectricity in magnetoelectric YMnO3. *Nature Materials*, *3*(3), 164–170. https://doi.org/10.1038/nmat1080

Vohs, J. M., & Gorte, R. J. (2009). High-performance SOFC cathodes prepared by infiltration. *Advanced Materials*, *21*(9), 943–956. https://doi.org/10.1002/adma.200802428

Wang, L., Merkle, R., Maier, J., Acartürk, T., & Starke, U. (2009). Oxygen tracer diffusion in dense Ba0.5Sr0.5Co 0.8Fe0.2O3-δ films. *Applied Physics Letters*, *94*(7), 2012–2015. https://doi.org/10.1063/1.3085969

Wei, B., Lü, Z., Huang, X., Miao, J., Sha, X., Xin, X., & Su, W. (2006). Crystal structure, thermal expansion and electrical conductivity of perovskite oxides BaxSr1-xCo0.8Fe0.2O3- δ (0.3 ≤ x ≤ 0.7). *Journal of the European Ceramic Society*, *26*(13), 2827–2832. https://doi.org/10.1016/j.jeurceramsoc.2005.06.047

Yuan, C., Luo, T., Li, J., Meng, X., Qian, J., Ye, X., Zhan, Z., Xia, C., & Wang, S. (2014). Infiltrated porous YSZ as a cathode active layer for cathode-supported solid oxide fuel cells. *Electrochemistry Communications*, *46*, 40–43. https://doi.org/10.1016/j.elecom.2014.05.031

Zhang, Y., Knibbe, R., Sunarso, J., Zhong, Y., Zhou, W., Shao, Z., & Zhu, Z. (2017). Recent Progress on Advanced Materials for Solid-Oxide Fuel Cells Operating Below 500 °C. *Advanced Materials*, *29*(48). https://doi.org/10.1002/adma.201700132

Zhao, T., Boullosa-Eiras, S., Yu, Y., Chen, D., Holmen, A., & Ronning, M. (2011). Synthesis of supported catalysts by impregnation and calcination of Low-temperature polymerizable metal-complexes. *Topics in Catalysis*, *54*(16–18), 1163–1174. https://doi.org/10.1007/s11244-011-9738-2

APPENDICES

Appendix A Data for the preparation of the precursor solution

To carry out the impregnation of 10 gram of YSZ8 in such a way that the material has a composition of 30% by weight of $YMnO_3$, the mass of $YMnO_3$ to be impregnated is determined.

$$1\ g\ YSZ * \frac{0.3\ g\ YMnO_3}{0.7\ g\ YSZ} = 0.4285\ g\ YMnO3$$

Based on the mass of yttrium manganite and in accordance with the stoichiometry:

$$Y_2O_3 + Mn_2O_3 \rightarrow 2YMnO_3$$

First the yttria nitrate must be for by the reaction of yttria oxide with nitric acid:

To prepare a 250ml of $Y(NO_3)_3$ at 1M

$$1\ M = \frac{n}{0.250\ L}$$

$$n = 0.250\ mol\ Y(NO_3)_3$$

$$Y_2O_3 + 6HNO_3 \rightarrow 2Y(NO_3)_3 + 2H_2O$$

Calculate the grams of Yttrium Oxide necessary for the reaction.

$$0.250\ mol\ Y(NO_3)_3 * \left(\frac{1\ mol\ Y_2O_3}{2\ mol\ Y(NO_3)_3}\right) * \left(\frac{225.81\ gY_2O_3}{1\ mol\ Y_2O_3}\right) = 28.2263\ g\ Y_2O_3$$

Calculate the grams of Nitric Acid necessary for the reaction.

$$0.250\ mol\ Y(NO_3)_3 * \left(\frac{6\ mol\ HNO_3}{2\ mol\ Y(NO_3)_3}\right) * \left(\frac{63.01\ gHNO_3}{1\ mol\ HNO_3}\right) = 47.2575\ g\ HNO_3$$

$$= 47.2575\ g\ HNO_3 * \left(\frac{100}{65}\right)$$

$$= 72.7038\ g\ HNO_3$$

Appendix B. Impregnation Process

To carry out the impregnation of 1 gram of YSZ8 so that the material attains a composition of 30 wt% $YMnO_3$, the mass of $YMnO_3$ to be impregnated is determined as follows:

$$1\ g\ YSZ * \frac{0.3\ g\ YMnO_3}{0.7\ g\ YSZ} = 0.4285\ g\ YMnO3$$

$$0.4285 g\ YMnO_3 * \frac{1\ mol\ YMnO_3}{196.841\ g\ YMnO_3} * \frac{1\ mol\ reactant}{2\ mol\ YMnO_3} = 1.088 * 10^{-3}\ mol$$

$$\frac{1.088 * 10^{-3}\ mol\ reactant}{mol\ of\ YMnO_3\ per\ impregnation} = number\ of\ impregnations\ (1)$$

Before starting the impregnation process, it was necessary to determine the incipient wetness volume of both sintered YSZ powders. This step allowed calculation of the number of moles of precursor incorporated in a single impregnation cycle, and estimation of how many cycles would be required to achieve a 30 wt% loading of $YMnO_3$ in YSZ.

Determine the number of moles in the incipient impregnation volume of YSZ sintered at 1200 °C

$$0.5\ M = \frac{n}{300\mu L}$$

$$n = \frac{0.5mol}{L} * 300\mu L * \frac{1L}{10^6\mu L}$$

$$n = 1.5 * 10^{-4}\ moles$$

$$\frac{1.088 * 10^{-3}\ moles\ of\ YMnO_3}{1.5 * 10^{-4} mol\ of\ YMnO_3} = 7.25\ times$$

Determine the number of moles in the incipient impregnation volume of YSZ sintered at 1300 °C

$$0.5M = \frac{n}{180\mu L}$$

$$n = \frac{0.5mol}{L} * 180\mu L * \frac{1L}{10^6\mu L}$$

$$n = 9 * 10^{-5}\ mol$$

$$\frac{1.088 * 10^{-3}\ mol\ of\ YMnO3}{9 * 10^{-5} mol\ of\ YMnO3} = 12.088\ times$$

Appendix C Graphical results of Rietveld refinements of (Y,Zr)MnO_3 synthetized over YSZ sintered for T_1=1200°C

Figure 1. Graphical result of Rietveld refinement of (Y,Zr)MnO3/YSZ-1200°C synthetized at 1000°C

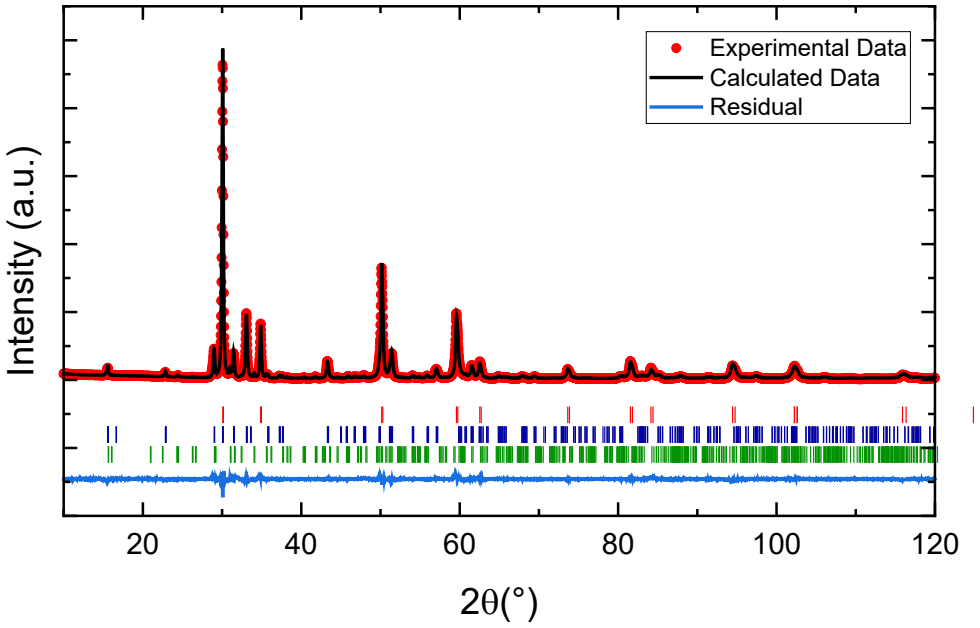

Figure 2. Graphical result of Rietveld refinement of (Y,Zr)MnO3/YSZ-1200°C synthetized at 1100°C

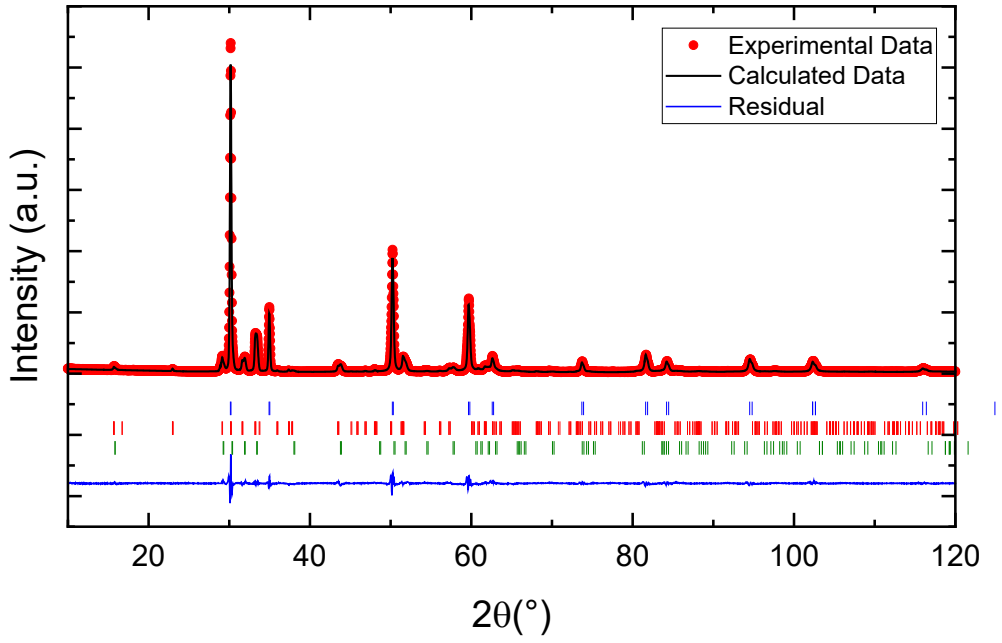

Figure 3. Graphical result of Rietveld refinement of (Y,Zr)MnO3/YSZ-1200°C synthetized at 1200°C

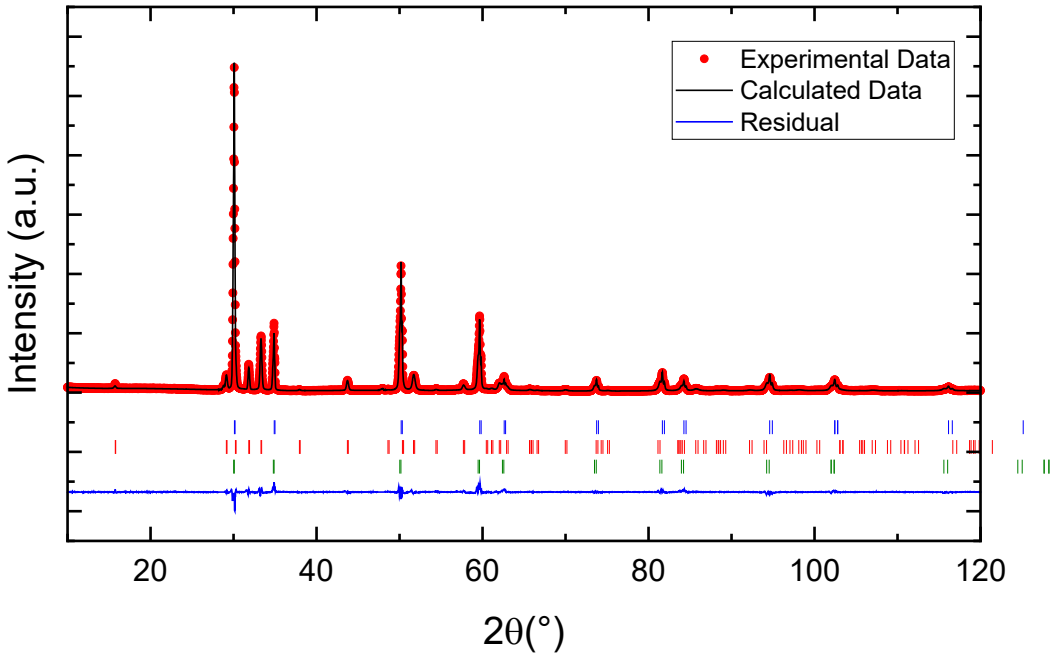

Appendix D Graphical results of Rietveld refinements of (Y,Zr)MnO_3 synthetized over YSZ sintered for T_1=1300°C

Figure 1. Graphical result of Rietveld refinement of (Y,Zr)MnO3/YSZ-1300°C synthetized at 1000°C

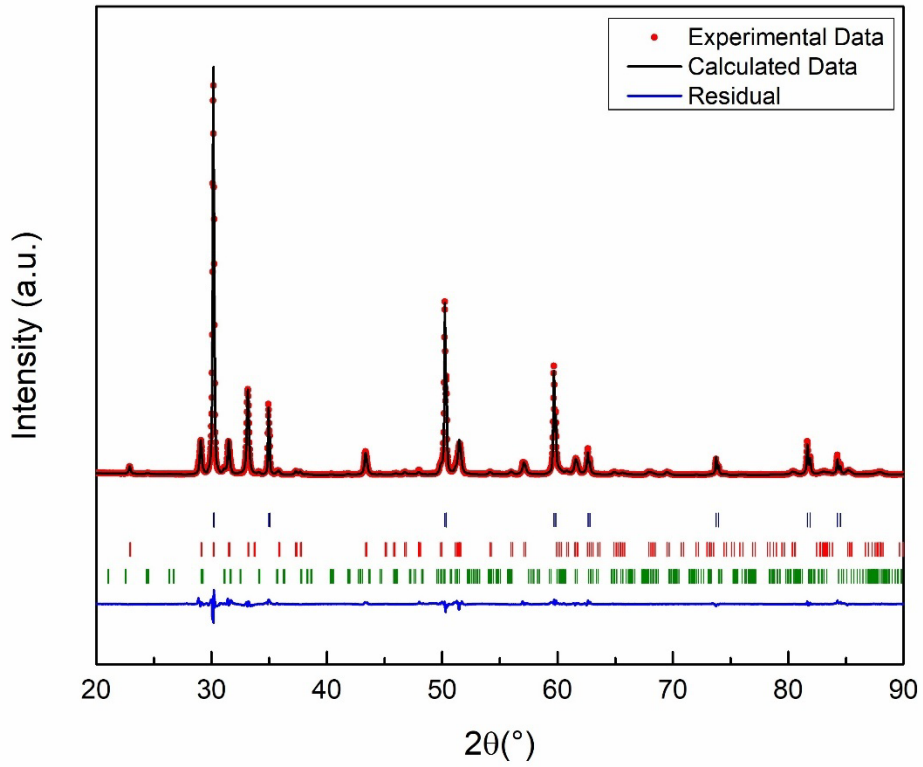

Figure 2. Graphical result of Rietveld refinement of (Y,Zr)MnO3/YSZ-1300°C synthetized at 1100°C

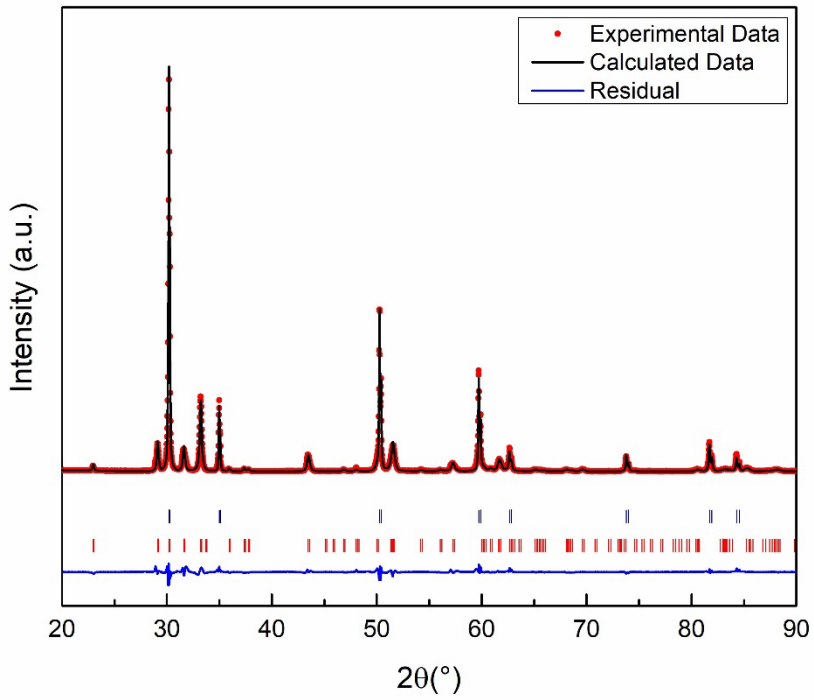

Figure 3. Graphical result of Rietveld refinement of (Y,Zr)MnO3/YSZ-1300°C synthetized at 1200°C

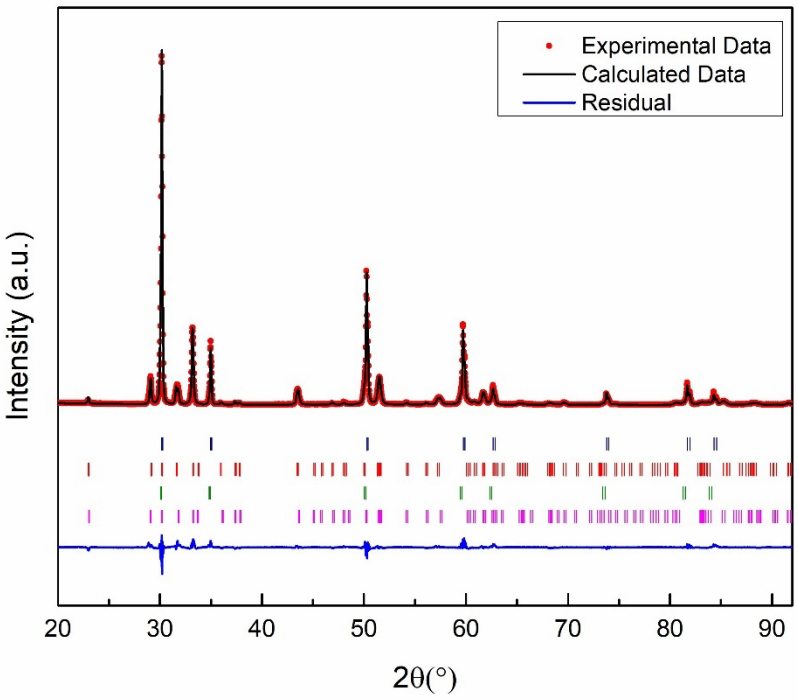

Appendix E Mathematical relationship between phases

As stated by Gibbs[1], since the parameters and the volume of the non-centrosymmetric and the centrosymmetric phases are mathematically related, this meaning that the two phases found in (Y,Zr)MnO_3 can be easily compared by:

a lattice parameter (P63cm):

$$a = \sqrt{3} * a' \text{ [=] Å}$$

c lattice parameter (P63cm):

$$c = c' \text{ [=] Å}$$

Volume (P63cm):

$$V = 3V' \text{ [=]Å}^3$$

Knowing that a', c' and V' are the cell parameters for the P63/mmc lattice.

[1] A. S. Gibbs, K. S. Knight, and P. Lightfoot, "High-temperature phase transitions of hexagonal YMnO3 Alexandra," Phys. Rev. B, vol. 83, no. 9, p. 94111, 2011